Journal of Positive Sciences (JPS) eISSN: 2582-9351, https://positive-sciences.com JPS. 2025 Nov; 7(5): 10-45

Article info
Received on: 03.09.2025
Accepted on: 26.10.2025
Published on: 30.11.2025
doi: https://doi.org/10.52688/ASP68339

Research Article

# Optimization of $ZrO_2$ nanoparticle Content for Superior Mechanical Behavior of 7075 Aluminum Composites

Haitham Mohammed Ibrahim Al-Zuhairi [1], Iqbal alshalal [2], Hind H. Abbood [3], Mohammed RASHEED [4, *]

[1, 2, 3] Training and Workshop Center, University of Technology- Iraq, Baghdad, Iraq
[4] Production Engineering & Metallurgy College, University of Technology- Iraq, Baghdad 10066, Iraq

[*] rasheed.mohammed40@yahoo.com

## ABSTRACT

7075 aluminum alloy is widely recognized as one of the most important lightweight structural materials for aerospace, automotive, and defense applications due to its excellent strength-to-weight ratio and favorable mechanical properties. However, its relatively limited wear resistance, moderate hardness, and susceptibility to localized deformation restrict its performance under severe service conditions. In the present study, zirconium dioxide ($ZrO_2$) nanoparticles were incorporated into a 7075 aluminum matrix to enhance its structural, mechanical, tribological, thermal, and corrosion properties. Four composite systems were fabricated using the powder metallurgy technique: unreinforced 7075 Al (S1), 7075Al + 1 wt.% $ZrO_2$ (S2), 7075Al + 3 wt.% $ZrO_2$ (S3), and 7075Al + 5 wt.% $ZrO_2$ (S4). Structural characterization by XRD confirmed the presence of α-Al and tetragonal $ZrO_2$ phases without undesirable reaction products. The average crystallite size decreased from 41.56 nm for S1 to 30.04 nm for S3, indicating significant grain refinement. FESEM, EDS, AFM, and TEM analyses revealed improved nanoparticle dispersion, reduced porosity, and enhanced interfacial bonding for the S3 composite. Density measurements showed a maximum density of 2.84 g $cm^{-3}$ and minimum porosity of 1.82% for S3. Mechanical characterization demonstrated that S3 exhibited the highest microhardness (≈182 HV), ultimate tensile strength (486 MPa), compressive strength (684 MPa), impact energy (18.9 J), nanohardness (3.85 GPa), and fatigue endurance limit (248 MPa). Tribological evaluation revealed the lowest wear loss (8.6 mg) and coefficient of friction (0.46) for S3. Furthermore, corrosion and thermal expansion analyses showed improved corrosion resistance and reduced coefficient of thermal expansion. Overall, the results demonstrate that 3 wt.% $ZrO_2$ is the optimum reinforcement content, providing the best balance between strength, toughness, wear resistance, thermal stability, and corrosion performance for advanced lightweight engineering applications.

**Keywords:** 7075 Aluminum alloy, $ZrO_2$ nanoparticles, aluminum matrix composites, mechanical properties, powder metallurgy

## INTRODUCTION

Among high-strength aluminum alloys, 7075 aluminum has attracted considerable attention because of its exceptional combination of low density and superior mechanical performance [1]. Since its development, this alloy has been extensively utilized in structural applications where weight reduction without sacrificing strength is a critical requirement. The alloy derives its outstanding properties primarily from its Zn–Mg–Cu alloying system, which provides excellent precipitation hardening capability and enables the production of components possessing high strength-to-weight ratios. Consequently, 7075 aluminum has become one of the most important engineering materials in modern manufacturing industries [2]. The unique characteristics of 7075 aluminum have led to its widespread application in aerospace, defense, and transportation sectors [3]. In aerospace structures, the alloy is commonly employed in aircraft fuselage components, wing structures,

*Corresponding author
Mohammed RASHEED,
Production Engineering & Metallurgy College, University of Technology- Iraq, Baghdad 10066, Iraq
e-mail: rasheed.mohammed40@yahoo.com

and landing gear systems due to its ability to withstand high stresses while minimizing structural weight. Similarly, defense industries utilize 7075 aluminum in armored systems and military equipment, whereas automotive and transportation industries increasingly adopt this alloy to improve fuel efficiency through vehicle lightweighting. The growing demand for high-performance and energy-efficient systems has further increased interest in enhancing the capabilities of this alloy [4]. Despite these advantages, 7075 aluminum exhibits several limitations that restrict its performance under severe operating conditions [5]. Although the alloy possesses excellent specific strength, good fatigue resistance, and favorable machinability, its relatively moderate wear resistance and limited surface hardness can lead to premature degradation when exposed to frictional contact and repetitive loading [6]. Furthermore, the alloy may experience reduced mechanical reliability under extreme loading environments, thereby limiting its long-term service performance. These shortcomings have motivated researchers to develop novel reinforcement strategies capable of improving the multifunctional behavior of 7075 aluminum alloys [7]. The incorporation of ceramic nanoparticles into aluminum matrices has emerged as an effective approach for overcoming the limitations associated with conventional aluminum alloys [8]. Among the available ceramic reinforcements, zirconium dioxide ($ZrO_2$) nanoparticles have attracted significant attention because of their high hardness, excellent thermal stability, superior wear resistance, and chemical inertness [9]. The nanoscale dimensions of $ZrO_2$ particles enable effective interaction with the metallic matrix, resulting in substantial modifications of the microstructure and mechanical response of the composite material [10]. One of the primary strengthening mechanisms induced by $ZrO_2$ nanoparticles is grain refinement. The presence of finely dispersed nanoparticles inhibits grain growth during processing and promotes the formation of finer matrix grains [11]. According to the Hall–Petch relationship, smaller grain sizes increase resistance to dislocation movement, thereby enhancing the strength and hardness of the material [12]. Additionally, the nanoparticles act as obstacles to dislocation motion through the Orowan strengthening mechanism, forcing dislocations to bypass the particles and increasing the stress required for plastic deformation [13]. Load transfer strengthening also contributes significantly to the improved mechanical performance of $ZrO_2$-reinforced aluminum composites. Under externally applied loads, part of the stress is transferred from the relatively soft aluminum matrix to the hard ceramic nanoparticles, thereby improving the overall load-bearing capability of the composite [14]. Moreover, differences in the coefficients of thermal expansion between aluminum and $ZrO_2$ generate geometrically necessary dislocations during cooling from processing temperatures, providing an additional thermal mismatch strengthening effect [15]. These mechanisms collectively contribute to enhanced hardness, improved wear resistance, and increased tensile and compressive strengths. Nevertheless, excessive nanoparticle additions may result in particle agglomeration due to the high surface energy associated with nanosized reinforcements [16]. Such agglomerates may act as stress concentration sites and increase porosity, leading to deterioration in ductility, toughness, and overall mechanical performance. Therefore, identifying the optimum $ZrO_2$ content remains essential for maximizing the benefits of nanoparticle reinforcement [17]. Although numerous investigations have explored the development of ceramic-reinforced aluminum matrix composites, determining the optimal concentration of $ZrO_2$ nanoparticles for maximizing the performance of 7075 aluminum remains a significant challenge [18]. The mechanical response of nanocomposites is strongly influenced by reinforcement content, particle distribution, and interfacial characteristics. While low reinforcement levels may provide insufficient strengthening [19], excessive additions frequently promote nanoparticle clustering, inadequate densification, and increased porosity. Consequently, the resulting composites may exhibit conflicting property trends, where improvements in hardness and strength are accompanied by reductions in ductility and impact resistance. Therefore, a systematic investigation aimed at identifying the optimum $ZrO_2$ nanoparticle concentration is required to achieve a balanced combination of mechanical properties suitable for practical engineering applications [20]. Despite the growing interest in nanoparticle-reinforced aluminum composites, relatively few studies have specifically addressed the optimization of $ZrO_2$ nanoparticle content in 7075 aluminum matrices. Existing investigations often focus on a limited number of properties, such as hardness or tensile strength, without considering the broader relationship between reinforcement content and multifunctional performance. Furthermore, comprehensive analyses involving multiple characterization techniques and mechanical evaluations remain scarce. The lack of systematic studies integrating microstructural observations with strengthening mechanisms has hindered the establishment of clear design guidelines for these advanced composites. Motivated by these limitations, the present study seeks to provide

*Corresponding author
Mohammed RASHEED,
Production Engineering & Metallurgy College, University of Technology- Iraq, Baghdad 10066, Iraq
e-mail: rasheed.mohammed40@yahoo.com

a comprehensive understanding of how $ZrO_2$ nanoparticle additions influence the structural and mechanical behavior of 7075 aluminum composites. By evaluating several reinforcement levels and correlating the observed properties with the underlying strengthening mechanisms, this work aims to identify an optimum $ZrO_2$ concentration capable of delivering superior mechanical performance suitable for industrial applications. The primary objective of this study is to fabricate and characterize $ZrO_2$ nanoparticle-reinforced 7075 aluminum matrix composites and determine the reinforcement level that provides the most favorable balance of mechanical properties. Particular emphasis is placed on understanding the influence of nanoparticle addition on microstructural evolution, strengthening behavior, and performance enhancement. To achieve these objectives, four composite systems were prepared using the powder metallurgy technique. The investigated compositions included unreinforced 7075 aluminum alloy (S1), 7075 aluminum reinforced with 1 wt.% $ZrO_2$ nanoparticles (S2), 3 wt.% $ZrO_2$ nanoparticles (S3), and 5 wt.% $ZrO_2$ nanoparticles (S4). Structural characterization and mechanical evaluations were subsequently performed to establish the relationship between reinforcement content and composite behavior. The novelty of the present work lies in the systematic optimization of $ZrO_2$ nanoparticle content within a 7075 aluminum matrix through comprehensive characterization and performance evaluation. Unlike previous investigations that focused on isolated mechanical properties, this study simultaneously examines hardness, tensile strength, compressive behavior, impact resistance, and wear performance to provide a holistic assessment of composite behavior. Furthermore, the study establishes direct correlations between microstructural features and the underlying strengthening mechanisms responsible for property enhancement. By identifying the optimum reinforcement concentration and clarifying the effects of nanoparticle dispersion and agglomeration, this work provides practical design guidelines for the development of lightweight structural composites with superior performance characteristics. Several limitations should be acknowledged in the present investigation. First, the reinforcement content was restricted to a range between 0 and 5 wt.% $ZrO_2$ nanoparticles, and higher concentrations were not considered. Second, only the powder metallurgy processing route was employed, while alternative fabrication techniques such as stir casting or additive manufacturing were beyond the scope of this work. In addition, the present study primarily focuses on room-temperature structural and mechanical properties, and elevated-temperature behavior was not investigated. Corrosion performance and long-term fatigue resistance were also excluded from the current study and may be addressed in future investigations to provide a more comprehensive understanding of the composite system. The remainder of this paper is organized as follows. Section 2 describes the materials used, composite fabrication procedures, and characterization techniques employed throughout the study. Section 3 presents and discusses the experimental results, including structural characterization, microstructural observations, and mechanical performance, together with the associated strengthening mechanisms. Finally, Section 4 summarizes the major findings of the investigation, highlights the practical implications of the results, and provides recommendations for future research directions aimed at further improving the performance of $ZrO_2$-reinforced 7075 aluminum composites.

## MATERIALS AND METHODS

### MATERIALS

Commercial 7075 aluminum alloy powder (purity: 99.5%, average particle size: 40–60 μm, molecular weight: 26.98 g $mol^{-1}$) was employed as the matrix material in the present investigation owing to its widespread use in high-performance structural applications. The alloy is primarily composed of aluminum with zinc, magnesium, and copper as the major alloying elements, providing excellent precipitation-hardening capability and superior strength-to-weight characteristics. The 7075 Al powder was purchased from Sigma-Aldrich (Merck KGaA, Darmstadt, Germany). Zirconium dioxide ($ZrO_2$) nanoparticles were selected as the reinforcing phase because of their high hardness, excellent thermal stability, superior wear resistance, and chemical inertness. The $ZrO_2$ nanoparticles possessed a purity of 99.9%, an average particle size of 20–40 nm, and a molecular weight of 123.22 g $mol^{-1}$. The nanoparticles were procured from Sigma-Aldrich (Merck KGaA, Darmstadt, Germany). Their nanoscale dimensions enabled effective interaction with the aluminum matrix and promoted multiple strengthening mechanisms, including grain refinement, Orowan strengthening, and load transfer strengthening. Prior to composite fabrication, both the matrix and

*Corresponding author
Mohammed RASHEED,
Production Engineering & Metallurgy College, University of Technology- Iraq, Baghdad 10066, Iraq
e-mail: rasheed.mohammed40@yahoo.com

reinforcement powders were dried at 80 °C for 12 h and stored in sealed containers under controlled laboratory conditions to minimize moisture absorption and contamination before processing.

## PREPARATION OF 7075AL–ZRO$_2$ COMPOSITES

The composites were fabricated using the powder metallurgy route due to its ability to achieve uniform reinforcement distribution and minimize undesirable interfacial reactions. Four compositions were prepared in this study, namely unreinforced 7075 aluminum alloy (S1), 7075 aluminum reinforced with 1 wt.% $ZrO_2$ nanoparticles (S2), 3 wt.% $ZrO_2$ nanoparticles (S3), and 5 wt.% $ZrO_2$ nanoparticles (S4). The required quantities of matrix and reinforcement powders were accurately weighed using a high-precision electronic balance according to the designed compositions. The powder mixtures were homogenized using a planetary ball mill to ensure uniform dispersion of the $ZrO_2$ nanoparticles within the aluminum matrix. The milling process was performed under controlled conditions using an appropriate ball-to-powder ratio and rotational speed to reduce particle agglomeration while preventing excessive cold welding of the aluminum particles. After mixing, the powders were dried and sieved to obtain a homogeneous feedstock suitable for compaction. Fig. 1 presents the schematic representation of the powder metallurgy route employed for the fabrication of 7075Al–$ZrO_2$ composites with different reinforcement contents. The process begins with the selection of high-purity 7075 aluminum powder and $ZrO_2$ nanoparticles, followed by precise powder weighing according to the designed compositions. The powders are subsequently homogenized using planetary ball milling to promote uniform dispersion of the ceramic nanoparticles and minimize agglomeration. The blended powders are then dried and sieved to obtain a homogeneous feedstock suitable for compaction. Uniaxial pressing is performed to produce green compacts, which are subsequently sintered under an inert atmosphere to improve densification and interparticle bonding. Finally, the sintered specimens are cooled to room temperature and prepared for structural characterization and mechanical evaluation. The figure also illustrates the four investigated compositions, namely S1 (0 wt.% $ZrO_2$), S2 (1 wt.% $ZrO_2$), S3 (3 wt.% $ZrO_2$), and S4 (5 wt.% $ZrO_2$), highlighting the systematic approach adopted to optimize the reinforcement content.

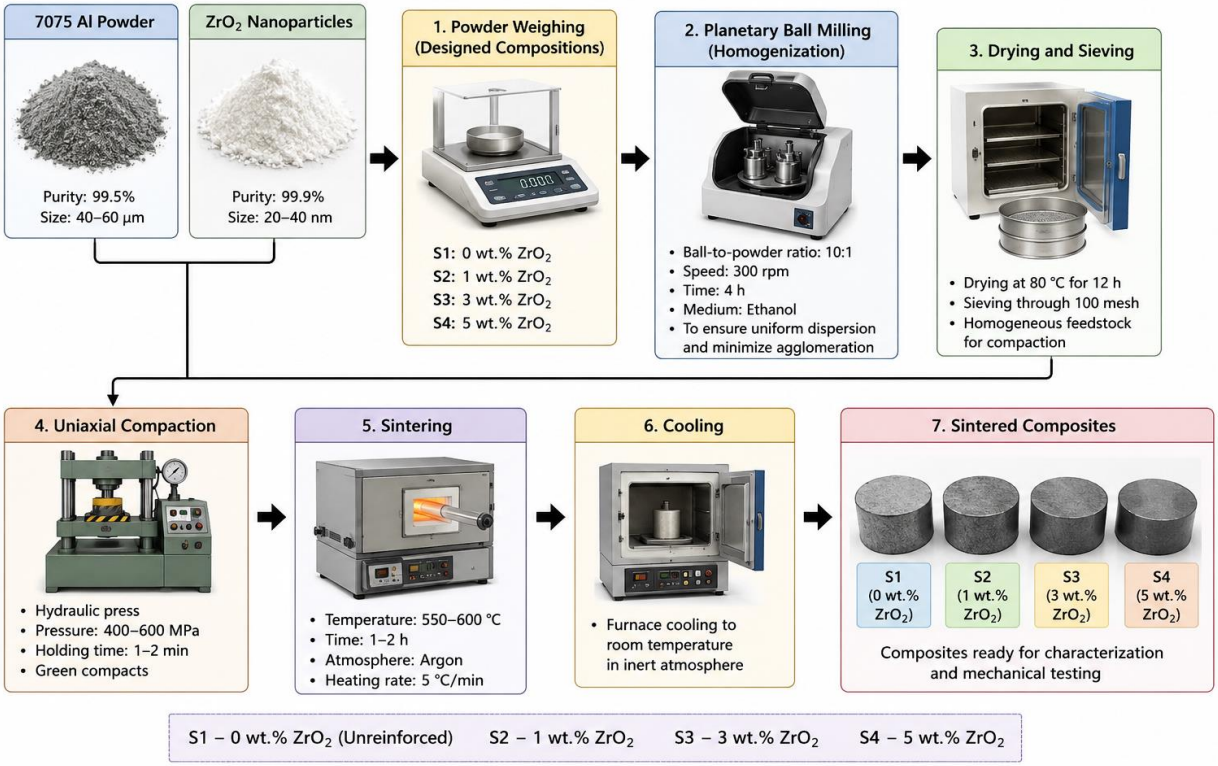


**Fig. 1.** Schematic illustration of the powder metallurgy fabrication process of 7075Al–$ZrO_2$ composites.

*Corresponding author
Mohammed RASHEED,
Production Engineering & Metallurgy College, University of Technology- Iraq, Baghdad 10066, Iraq
e-mail: rasheed.mohammed40@yahoo.com

## POWDER COMPACTION AND SINTERING

The blended powders were compacted using a uniaxial hydraulic press equipped with a hardened steel die to produce cylindrical specimens with the desired dimensions. A compaction pressure ranging from 400 to 600 MPa was applied and maintained for a specified holding period to improve green density and particle bonding. The resulting green compacts were carefully removed from the die and subsequently sintered in a controlled-atmosphere furnace to enhance densification and metallurgical bonding. Sintering was carried out at temperatures between 550 and 600 °C for 1–2 h under an inert atmosphere to minimize oxidation of the aluminum matrix. After completion of the sintering process, the specimens were allowed to cool gradually to room temperature inside the furnace. The sintered composites were then machined and polished according to the requirements of the subsequent characterization and mechanical testing procedures. Fig. 2 presents the schematic representation of the powder compaction and sintering procedures employed in the fabrication of 7075Al–$ZrO_2$ composites using the powder metallurgy technique. The figure illustrates the sequential processing stages beginning with the uniaxial compaction of the blended powders using a hydraulic press equipped with a hardened steel die to produce cylindrical green compacts. A compaction pressure of 400–600 MPa was applied for a holding period of 1–2 min to enhance green density and improve particle bonding. The green specimens were subsequently subjected to sintering in a controlled-atmosphere furnace at temperatures ranging from 550 to 600 °C for 1–2 h under an argon atmosphere to promote densification while minimizing oxidation of the aluminum matrix. After sintering, the specimens were allowed to cool gradually inside the furnace to room temperature in order to reduce residual stresses and avoid thermal shock. The figure also summarizes the investigated composite compositions and the principal processing parameters adopted throughout the study prior to machining, polishing, characterization, and mechanical testing

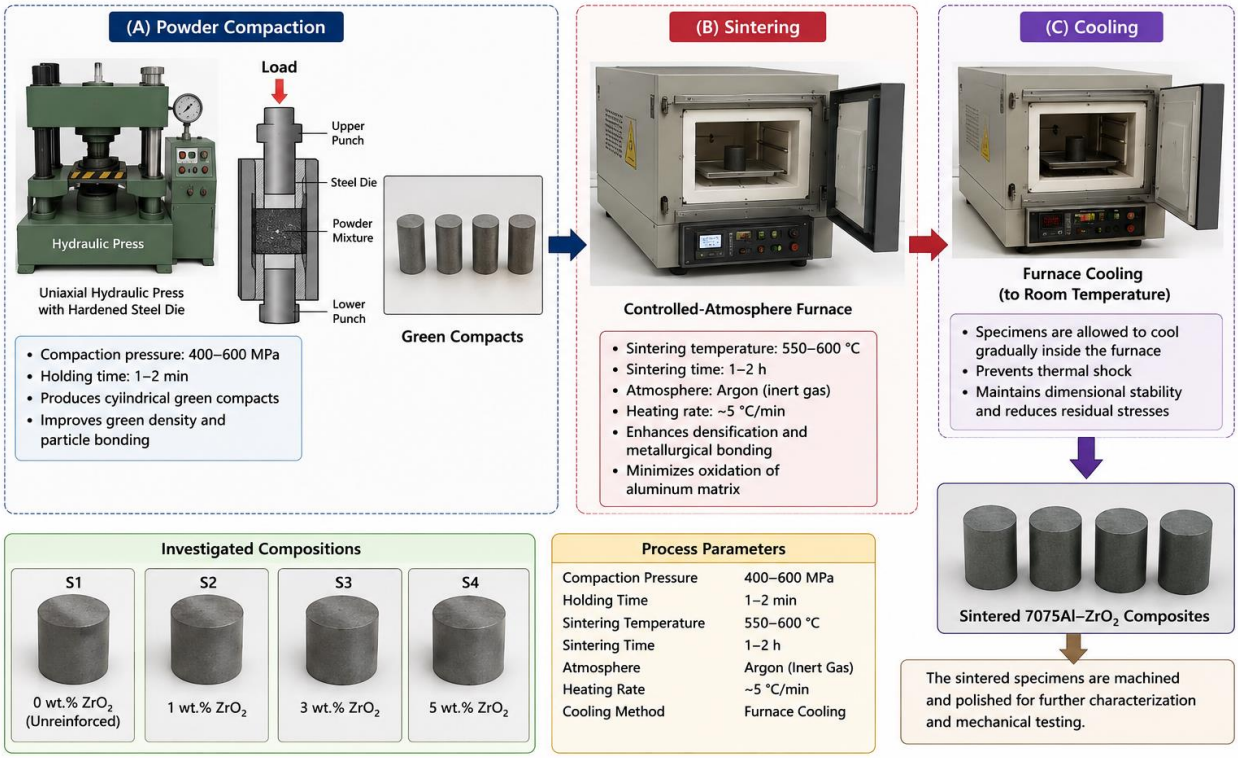


**Fig. 2.** Schematic illustration of the powder compaction and sintering process used for the fabrication of 7075Al–$ZrO_2$ composites

## SAMPLE DESIGNATION

The fabricated composites were designated according to their $ZrO_2$ nanoparticle content. The sample nomenclature adopted throughout this study is presented in Table 1.

*Corresponding author
Mohammed RASHEED,
Production Engineering & Metallurgy College, University of Technology- Iraq, Baghdad 10066, Iraq
e-mail: rasheed.mohammed40@yahoo.com

**Table 1.** Composition of the fabricated 7075Al–$ZrO_2$ composites.

| Sample | Composition |
|---|---|
| S1 | 7075 Al alloy (0 wt.% $ZrO_2$) |
| S2 | 7075 Al + 1 wt.% $ZrO_2$ |
| S3 | 7075 Al + 3 wt.% $ZrO_2$ |
| S4 | 7075 Al + 5 wt.% $ZrO_2$ |

## STRUCTURAL AND MICROSTRUCTURAL CHARACTERIZATION

The phase constitution of the fabricated composites was investigated using an X-ray diffractometer (XRD, X'Pert PRO MPD, PANalytical B.V., Almelo, The Netherlands) equipped with Cu Kα radiation (λ = 1.5406 Å) operating at 40 kV and 40 mA. Diffraction patterns were recorded over a 2θ range of 20°–80° with a step size of 0.02° and a scanning rate of 2° $min^{-1}$. The obtained diffraction data were employed to identify the crystalline phases present in the composites and to evaluate the influence of $ZrO_2$ nanoparticle reinforcement on the structural characteristics of the 7075 aluminum matrix. The average crystallite size was estimated using the Scherrer equation. Field emission scanning electron microscopy (FESEM, JSM-7610F Plus, JEOL Ltd., Tokyo, Japan) operated at an accelerating voltage of 5–20 kV was utilized to examine the surface morphology, grain characteristics, nanoparticle distribution, and interfacial bonding between the aluminum matrix and $ZrO_2$ nanoparticles. The microscope provided a magnification range of approximately ×25 to ×1,000,000 with a spatial resolution of 1.0 nm at 15 kV. Energy-dispersive X-ray spectroscopy (EDS, X-MaxN 80, Oxford Instruments, Abingdon, United Kingdom) coupled with elemental mapping was employed to determine the elemental composition and assess the homogeneity of $ZrO_2$ dispersion throughout the matrix. The EDS system allowed elemental detection over an energy range of 0–20 keV. Atomic force microscopy (AFM, Dimension Icon, Bruker Corporation, Billerica, MA, USA) operating in tapping mode was used to obtain three-dimensional surface topography and quantify surface roughness parameters, including the average roughness (Ra) and root mean square roughness (Rq). Surface scans were acquired over areas ranging from 1 × 1 $\mu m^2$ to 20 × 20 $\mu m^2$, with a vertical resolution better than 0.1 nm. Transmission electron microscopy (TEM, JEM-2100, JEOL Ltd., Tokyo, Japan) operated at an accelerating voltage of 200 kV was employed to investigate the nanoscale distribution of the reinforcement phase, evaluate the matrix–particle interfacial characteristics, and identify possible nanoparticle agglomeration within the composites. The instrument provided a point resolution of 0.23 nm and a lattice resolution of 0.14 nm, enabling detailed observation of the nanostructural features of the fabricated composites.

## DENSITY AND POROSITY MEASUREMENTS

The experimental density of the sintered specimens was determined using the Archimedes principle in accordance with ASTM B962. Theoretical density values were calculated using the rule of mixtures based on the constituent materials and their respective weight fractions. The percentage porosity of each composite was subsequently estimated from the difference between the theoretical and experimental densities. These measurements provided valuable information regarding the effectiveness of the consolidation process and the influence of $ZrO_2$ content on densification behavior. Fig. 3 presents a schematic illustration of the density and porosity measurement procedure performed according to the ASTM B962 standard using the Archimedes principle. The method involves weighing the sintered composite specimens in air to obtain the dry mass, followed by immersion in distilled water to determine the suspended mass and saturated mass. These measurements were subsequently used to calculate the experimental density of the composites. The theoretical density was estimated using the rule of mixtures based on the densities and weight fractions of the constituent materials, namely 7075 aluminum alloy and $ZrO_2$ nanoparticles. The percentage porosity was then determined from the difference between the theoretical and experimental densities. This approach provides a reliable assessment of the effectiveness of powder consolidation and sintering, while also revealing the influence of $ZrO_2$ nanoparticle addition on densification behavior. Lower porosity and higher relative density generally indicate improved particle bonding and enhanced structural integrity of the fabricated composites.

*Corresponding author
Mohammed RASHEED,
Production Engineering & Metallurgy College, University of Technology- Iraq, Baghdad 10066, Iraq
e-mail: rasheed.mohammed40@yahoo.com

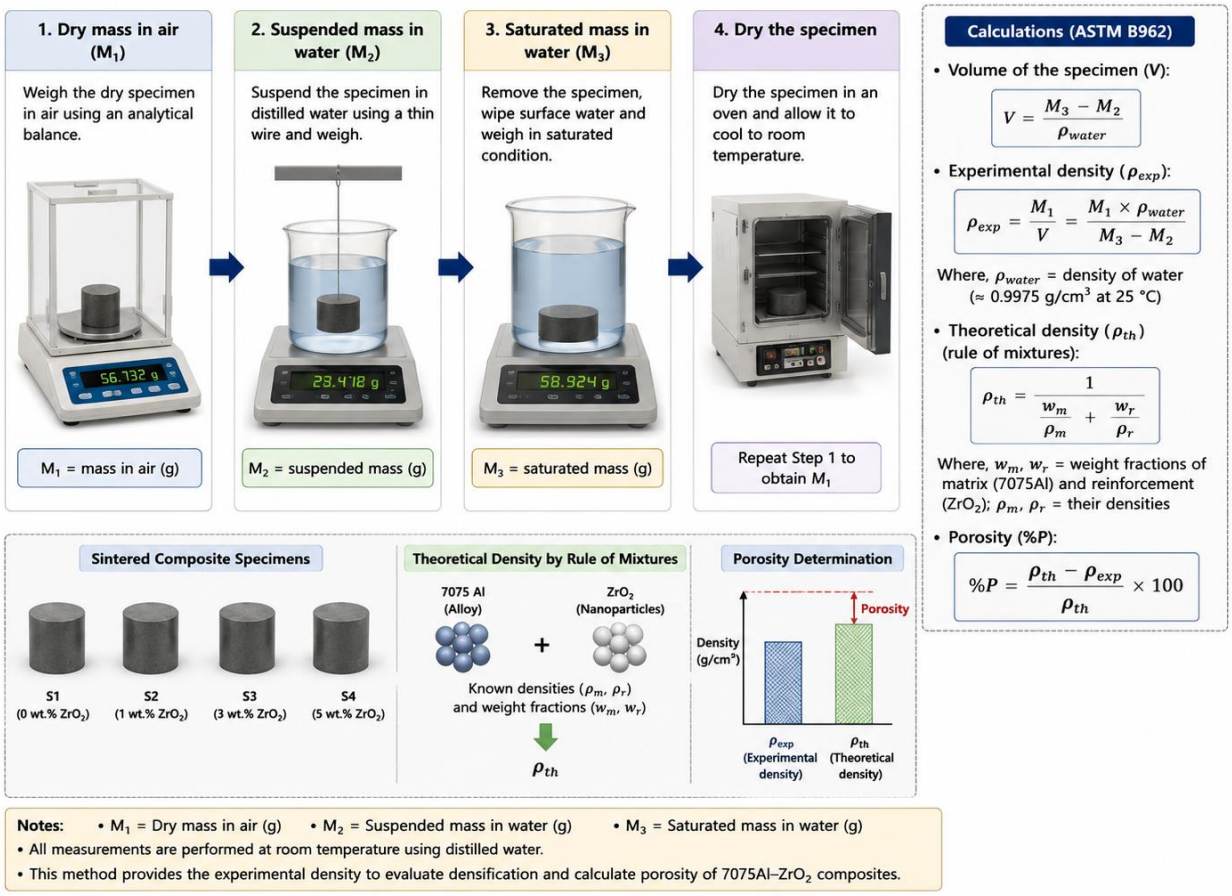


**Fig. 3.** Schematic representation of density and porosity measurements of the sintered 7075Al–$ZrO_2$ composites according to ASTM B962 using the Archimedes principle.

## MECHANICAL CHARACTERIZATION

The mechanical performance of the fabricated 7075Al–$ZrO_2$ composites was systematically evaluated using a series of standardized testing methods to investigate the influence of $ZrO_2$ nanoparticle reinforcement on hardness, strength, toughness, fatigue resistance, and high-temperature behavior. Vickers microhardness measurements were performed according to ASTM E384 using a Vickers microhardness tester (HMV-G21DT, Shimadzu Corporation, Kyoto, Japan) equipped with a diamond pyramidal indenter. The tests were conducted under a constant load of 500 g (HV0.5) with a dwell time of 15 s. At least five indentations were made at different locations on each specimen to ensure measurement reliability, and the average hardness value was reported. The instrument provides a load range of 10–2000 g and an optical measurement resolution of 0.01 µm. The tensile properties of the composites were evaluated according to ASTM E8/E8M using a universal testing machine (Instron 5982, Instron Corporation, Norwood, MA, USA) equipped with a 100 kN load cell. Tensile tests were carried out at room temperature using a crosshead speed of 1 mm $min^{-1}$. The measured mechanical parameters included ultimate tensile strength (UTS), yield strength (YS), Young's modulus (E), and percentage elongation (%EL). The testing system provides a force measurement accuracy better than ±0.5% and a displacement resolution of 0.01 mm. Compression testing was conducted according to ASTM E9 using the same Instron 5982 universal testing machine fitted with compression platens and a 100 kN load cell. The tests were performed under uniaxial loading conditions at a crosshead speed of 1 mm $min^{-1}$ to determine the compressive yield strength, ultimate compressive strength, and deformation behavior of the fabricated composites. The use of the same testing platform ensured consistency and comparability between tensile and compression measurements. Impact toughness was evaluated using a Charpy impact testing machine (JBW-300B, Jinan Testing Equipment Co., Ltd., Jinan, China) in accordance with ASTM E23. Standard V-notched specimens were tested at room temperature, and the absorbed impact energy was recorded to assess the resistance of the composites to sudden fracture and dynamic loading. Nanoindentation measurements were carried out using a nanoindenter (TI 980 TriboIndenter, Bruker Corporation,

*Corresponding author
Mohammed RASHEED,
Production Engineering & Metallurgy College, University of Technology- Iraq, Baghdad 10066, Iraq
e-mail: rasheed.mohammed40@yahoo.com

Minneapolis, MN, USA) equipped with a Berkovich diamond tip. The tests were performed following the Oliver–Pharr method to determine nanohardness, reduced elastic modulus, and load–displacement behavior. Multiple indentations were conducted on each specimen to ensure statistical reliability. The fatigue behavior of the composites was investigated using a rotating bending fatigue testing machine (Model HSM19, Hi-Tech Machine Inc., Tokyo, Japan) according to ASTM E466. Fatigue tests were performed under fully reversed loading conditions (R = −1) at room temperature. The number of cycles to failure was recorded at different stress amplitudes to establish the S–N curves and determine the endurance limit of each composite. High-temperature mechanical testing was performed using a universal testing machine equipped with a high-temperature furnace attachment (Instron 5982 with environmental chamber, Instron Corporation, Norwood, MA, USA). Compression tests were conducted at 25, 100, 200, and 300°C to evaluate the thermal stability and strength-retention capability of the composites under elevated-temperature service conditions. Fig. 4 presents a schematic overview of the mechanical characterization techniques employed to evaluate the performance of the fabricated 7075Al–$ZrO_2$ composites. The figure summarizes the Vickers hardness, tensile, compression, impact, nanoindentation, fatigue, and high-temperature mechanical tests used to investigate the influence of $ZrO_2$ nanoparticle reinforcement on the overall mechanical behavior of the composites. Collectively, these characterization techniques provide a comprehensive assessment of the strengthening and toughening mechanisms associated with the incorporation of $ZrO_2$ nanoparticles into the 7075 aluminum matrix.

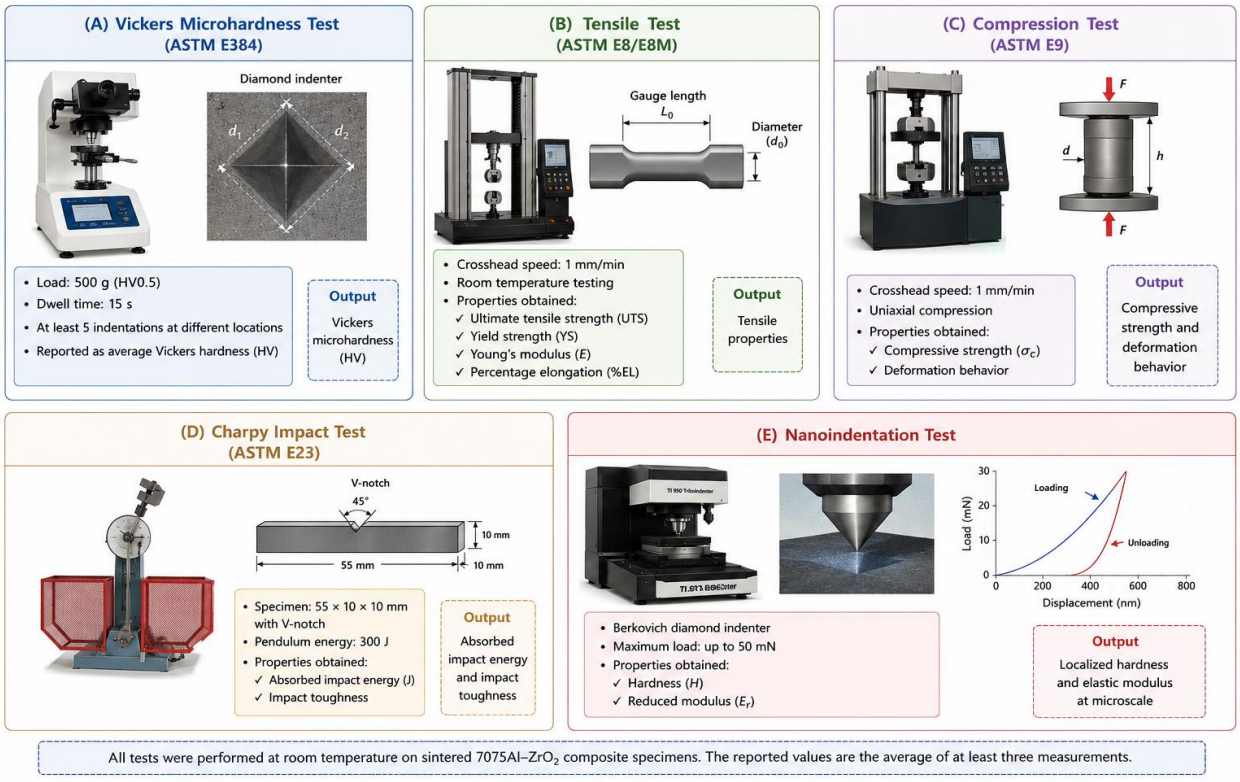


**Fig. 4.** Schematic illustration of the mechanical characterization methods used for evaluating the performance of 7075Al–$ZrO_2$ composites: (A) Vickers microhardness test (ASTM E384), (B) tensile test (ASTM E8/E8M), (C) compression test (ASTM E9), (D) Charpy impact test (ASTM E23), and (E) nanoindentation analysis.

## TRIBOLOGICAL EVALUATION

The dry sliding wear behavior of the fabricated composites was investigated using a pin-on-disc tribometer (TR-20LE, Ducom Instruments Pvt. Ltd., Bengaluru, India) in accordance with ASTM G99. The wear tests were conducted under controlled conditions using predetermined normal loads, sliding velocities, and sliding distances to evaluate the tribological response of the fabricated specimens. Cylindrical pins machined from the sintered composites were brought into contact with a hardened steel disc under dry sliding conditions. The wear loss was determined from the mass difference of the specimens before and after testing using a high-precision analytical balance, while the specific wear rate was calculated based on the applied load and total sliding distance. The tribometer is capable of operating under normal loads ranging

*Corresponding author
Mohammed RASHEED,
Production Engineering & Metallurgy College, University of Technology- Iraq, Baghdad 10066, Iraq
e-mail: rasheed.mohammed40@yahoo.com

from 1 to 200 N, rotational speeds of 50–2000 rpm, and sliding distances up to 10,000 m. Simultaneously, the coefficient of friction (COF) was continuously monitored and recorded throughout the experiments to assess frictional stability and investigate the influence of $ZrO_2$ nanoparticle reinforcement on the sliding behavior of the composites. **Fig. 5** presents the schematic illustration of the pin-on-disc wear testing arrangement employed to evaluate the tribological performance of the fabricated 7075Al–$ZrO_2$ composites in accordance with ASTM G99. The figure demonstrates the experimental configuration in which the composite pin specimen is pressed against a rotating hardened steel disc under a predetermined normal load. During sliding, the frictional force generated at the contact interface is continuously monitored to determine the coefficient of friction, while the wear loss is measured from the mass change of the specimens before and after testing. The experimental setup also highlights the principal testing parameters, including the applied load, sliding speed, sliding distance, and wear track radius, which collectively govern the wear behavior of the investigated composites. The obtained results provide valuable insights into the effect of $ZrO_2$ nanoparticle reinforcement on the wear resistance and frictional characteristics of 7075 aluminum matrix composites.

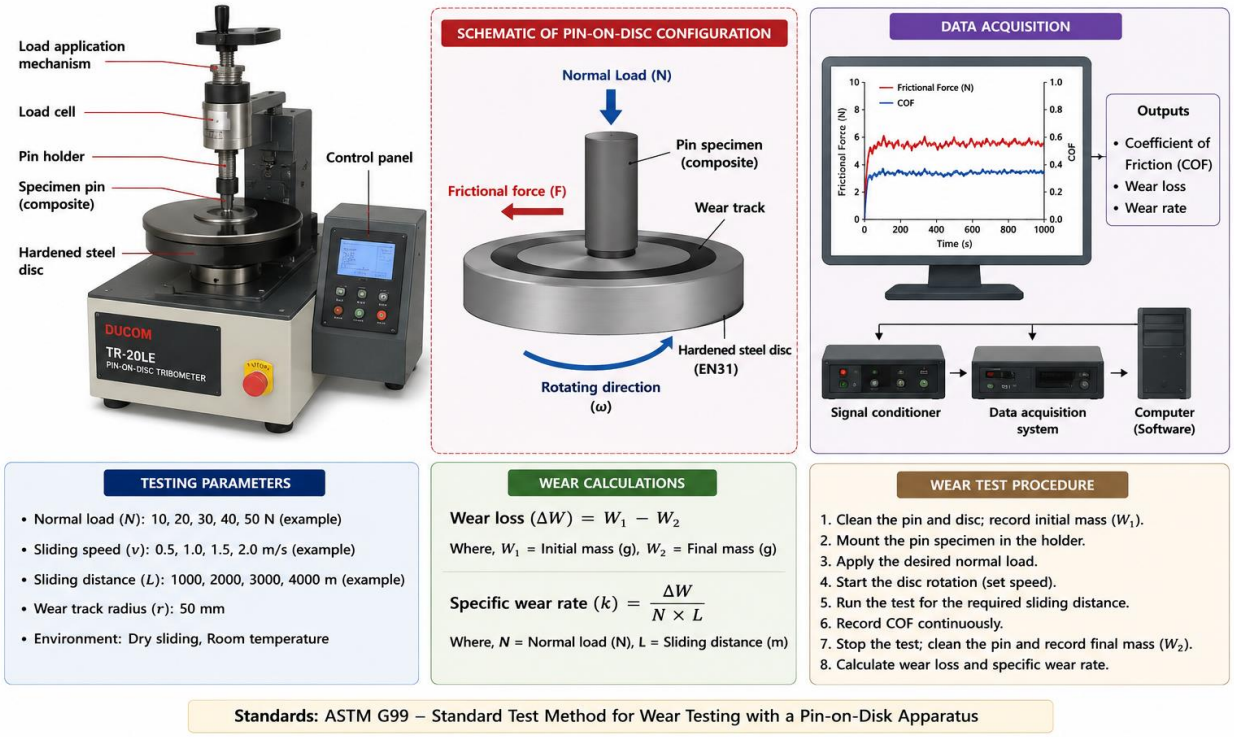


**Fig. 5.** Schematic representation of the pin-on-disc tribological test setup used for evaluating the dry sliding wear behavior of 7075Al–$ZrO_2$ composites according to ASTM G99.

## DATA ANALYSIS AND STATISTICAL EVALUATION

All experimental measurements were performed in triplicate to ensure reproducibility and reliability. The obtained results were expressed as mean values accompanied by their corresponding standard deviations. Comparative analyses were carried out to evaluate the influence of $ZrO_2$ nanoparticle content on the various physical and mechanical properties of the composites. The experimental findings were subsequently correlated with the observed microstructural characteristics and strengthening mechanisms to identify the optimum reinforcement level capable of delivering superior overall performance.

*Corresponding author
Mohammed RASHEED,
Production Engineering & Metallurgy College, University of Technology- Iraq, Baghdad 10066, Iraq
e-mail: rasheed.mohammed40@yahoo.com

## RESULTS AND DISCUSSION

## STRUCTURAL CHARACTERIZATION

## X-RAY DIFFRACTION (XRD)

Fig. 6 presents the X-ray diffraction patterns of the fabricated 7075Al–$ZrO_2$ composites containing different reinforcement contents, namely S1 (7075 Al, 0 wt.% $ZrO_2$), S2 (7075 Al + 1 wt.% $ZrO_2$), S3 (7075 Al + 3 wt.% $ZrO_2$), and S4 (7075 Al + 5 wt.% $ZrO_2$). The XRD analysis confirmed that all investigated composites were predominantly composed of an aluminum-rich matrix accompanied by the characteristic reflections of zirconium dioxide nanoparticles. The dominant phase identified in all diffraction patterns was the α-Al phase, indexed according to JCPDS/PDF card No. 04-0787 [21]. This phase possesses a face-centered cubic (FCC) crystal structure with a lattice parameter of approximately a ≈ 4.049 Å, belonging to the Fm-3m space group and the cubic crystal system. The principal α-Al diffraction peaks appeared at approximately 38.47°, 44.74°, 65.13°, and 78.22°, corresponding to the (111), (200), (220), and (311) crystallographic planes, respectively. Because α-Al exhibits cubic symmetry, the crystallographic angles satisfy the relationship α = β = γ = 90°. The persistence of these characteristic peaks in all specimens indicates that the incorporation of $ZrO_2$ nanoparticles did not alter the fundamental crystal structure of the 7075 aluminum matrix [22]. In addition to the aluminum matrix reflections, diffraction peaks corresponding to $ZrO_2$ nanoparticles were detected in the reinforced composites and indexed according to JCPDS/PDF card No. 17-0923. The zirconia phase exhibited a tetragonal crystal structure with lattice parameters of approximately a ≈ 3.60 Å and c ≈ 5.18 Å, belonging to the $P4_2/nmc$ space group. The characteristic $ZrO_2$ reflections appeared at approximately 30.22°, 35.22°, 50.32°, 60.18°, and 74.84°, corresponding to the (101), (110), (112), (211), and (220) crystallographic planes, respectively. The intensity of these reflections progressively increased from S2 to S4 as the reinforcement content increased, confirming the successful incorporation of $ZrO_2$ nanoparticles within the aluminum matrix. Furthermore, no additional diffraction peaks associated with undesirable reaction products were observed, suggesting that the powder metallurgy process and sintering conditions did not induce significant interfacial reactions between the matrix and reinforcement phases [23].
The diffraction patterns further revealed that increasing the $ZrO_2$ content influenced both the relative peak intensities and peak broadening of the existing phases. The unreinforced alloy (S1) exhibited sharp α-Al reflections with relatively narrow peak widths, indicating good crystallinity and low defect concentration within the aluminum matrix. Upon the addition of 1 wt.% $ZrO_2$ (S2), slight peak broadening became evident, reflecting the introduction of lattice distortions associated with the thermal expansion mismatch between the aluminum matrix and the ceramic nanoparticles [24]. The composite reinforced with 3 wt.% $ZrO_2$ (S3) exhibited the most uniform peak profiles and well-defined diffraction intensities, indicating effective nanoparticle dispersion and enhanced structural homogeneity. However, further increasing the reinforcement content to 5 wt.% $ZrO_2$ (S4) resulted in moderate peak broadening, which may be attributed to localized strain accumulation and the onset of nanoparticle agglomeration. These observations suggest that moderate $ZrO_2$ additions improve the crystallographic quality of the composites, whereas excessive reinforcement may introduce additional lattice imperfections [25]. The structural parameters summarized in Table 1 provide quantitative support for these observations. The interplanar spacing values were determined using Bragg's law, $n\lambda = 2d\sin\theta$, where n is the diffraction order, λ is the wavelength of the Cu Kα radiation (1.5406 Å), d is the interplanar spacing, and θ is the Bragg angle. The crystallite size was estimated using the Debye–Scherrer equation, $D_{cs} = K\lambda/\beta cos\theta$, where $K$ is the shape factor (0.9), $\lambda$ is the X-ray wavelength, $\beta$ is the full width at half maximum ($FWHM$) expressed in radians, and $\theta$ is the diffraction angle. The average crystallite size decreased progressively from 41.56 nm in the unreinforced alloy (S1) to 34.73 nm in S2 and reached a minimum value of 30.04 nm in the composite containing 3 wt.% $ZrO_2$ (S3), corresponding to an overall reduction of approximately 27.7% relative to S1. This reduction in crystallite size reflects the grain refinement effect induced by the uniformly dispersed nanoparticles, which effectively restricted grain growth during sintering. For the S4 composite, the average crystallite size increased slightly to 32.53 nm, suggesting that partial nanoparticle agglomeration reduced the efficiency of grain boundary pinning. For example, the crystallite size associated with the α-Al (111) reflection decreased from 41.04 nm in S1 to 36.58 nm in S2 and further to 31.17 nm in S3 before increasing to 34.35 nm in S4. These findings

*Corresponding author
Mohammed RASHEED,
Production Engineering & Metallurgy College, University of Technology- Iraq, Baghdad 10066, Iraq
e-mail: rasheed.mohammed40@yahoo.com

demonstrate that the 3 wt.% $ZrO_2$ reinforcement level provided the greatest crystallographic refinement among the investigated composites [26, 27]. The defect-related parameters summarized in Table 2 provide further insight into the influence of $ZrO_2$ nanoparticle reinforcement on the crystallographic quality of the fabricated composites. The lattice microstrain values were calculated using $\varepsilon = \beta/4\tan\theta$, where $\beta$ represents the peak broadening and $\theta$ is the diffraction angle, whereas the dislocation density was estimated from $\delta = 1/Dcs^2$ [28]. The unreinforced alloy (S1) exhibited the lowest microstrain values because of the absence of ceramic reinforcement and the relatively undisturbed aluminum lattice. The addition of $ZrO_2$ nanoparticles increased the lattice strain owing to the thermal expansion mismatch between the matrix and reinforcement, which generated additional geometrically necessary dislocations. The S2 composite exhibited moderate microstrain values ranging from approximately $1.50 \times 10^{-3}$ to $4.61 \times 10^{-3}$. The highest microstrain values were observed for S3, ranging from approximately $1.72 \times 10^{-3}$ to $5.33 \times 10^{-3}$, indicating the strongest interaction between the matrix and the uniformly distributed nanoparticles. In contrast, S4 exhibited slightly lower values ranging from $1.61 \times 10^{-3}$ to $4.92 \times 10^{-3}$, suggesting that nanoparticle clustering partially reduced the effectiveness of strain generation. A similar trend was observed for the dislocation density values. The S1 alloy exhibited the lowest dislocation density values, ranging from approximately $0.52 \times 10^{-3}$ to $0.62 \times 10^{-3}$ $nm^{-2}$, whereas S2 exhibited values between $0.66 \times 10^{-3}$ and $1.20 \times 10^{-3}$ $nm^{-2}$. The S3 composite displayed the highest dislocation density values, ranging from approximately $0.88 \times 10^{-3}$ to $1.61 \times 10^{-3}$ $nm^{-2}$, indicating enhanced resistance to dislocation motion and consequently superior strengthening. The S4 composite exhibited intermediate values ranging from $0.75 \times 10^{-3}$ to $1.37 \times 10^{-3}$ $nm^{-2}$, reflecting the adverse influence of excessive reinforcement additions [29, 30]. The preferred crystallographic orientation of the fabricated composites was evaluated using the texture coefficient (TC), which provides quantitative information regarding the tendency of crystallites to grow preferentially along specific crystallographic planes relative to the standard powder diffraction pattern [31]. The texture coefficient was calculated according to the following relationship: $TC(hkl) = \frac{\frac{I(hkl)}{I_O(hkl)}}{\frac{1}{N}\sum_{i=1}^{N}\frac{I(hkl)}{I_O(hkl)}}$ ,where $I(hkl)$ is the experimentally measured intensity of the diffraction peak corresponding to the $(hkl)$ plane, $I_0(hkl)$ is the standard intensity obtained from the reference JCPDS/PDF database, and N represents the total number of reflections considered in the calculation. A texture coefficient value close to unity indicates random orientation of the crystallites, whereas values greater than unity indicate the existence of preferred orientation along a particular crystallographic plane. The unreinforced alloy (S1) exhibited nearly random crystallographic orientation, with TC values ranging from approximately 0.95 to 1.05. The addition of 1 wt.% $ZrO_2$ slightly enhanced the degree of preferred orientation, and the TC values increased to approximately 0.88–1.09. The strongest preferred orientation was observed for the S3 composite, where the TC values ranged from approximately 1.03 to 1.15. In particular, the α-Al (200) and $ZrO_2$ (101) reflections exhibited the highest texture coefficients, indicating that the homogeneous distribution of nanoparticles promoted preferential crystallographic growth and improved structural ordering. In contrast, the S4 composite exhibited TC values between approximately 0.96 and 1.21. Although certain reflections retained preferred orientation characteristics, the overall texture intensity decreased compared with S3, indicating that excessive nanoparticle additions partially disturbed the uniformity of crystallographic development [32].

Finally, the unit-cell volumes listed in Table 2 exhibited only negligible variations among the investigated composites. The α-Al phase maintained unit-cell volumes ranging from approximately 66.16 to 66.43 $Å^3$, whereas the tetragonal $ZrO_2$ phase exhibited values close to 67.13–67.31 $Å^3$. These minor differences indicate that the incorporation of $ZrO_2$ nanoparticles did not significantly alter the intrinsic crystal structures of either phase but primarily influenced the defect structure and crystallographic refinement of the composites. Therefore, the combined interpretation of Fig. 6, Table 1, and Table 2 confirms that the composite reinforced with 3 wt.% $ZrO_2$ nanoparticles (S3) possessed the most favorable structural characteristics, characterized by refined crystallite size, enhanced defect-mediated strengthening, increased dislocation density, and stronger preferred orientation. These structural modifications provide a clear explanation for the superior mechanical and tribological performance expected for the optimally reinforced 7075Al–3 wt.% $ZrO_2$ composite.

*Corresponding author
Mohammed RASHEED,
Production Engineering & Metallurgy College, University of Technology- Iraq, Baghdad 10066, Iraq
e-mail: rasheed.mohammed40@yahoo.com

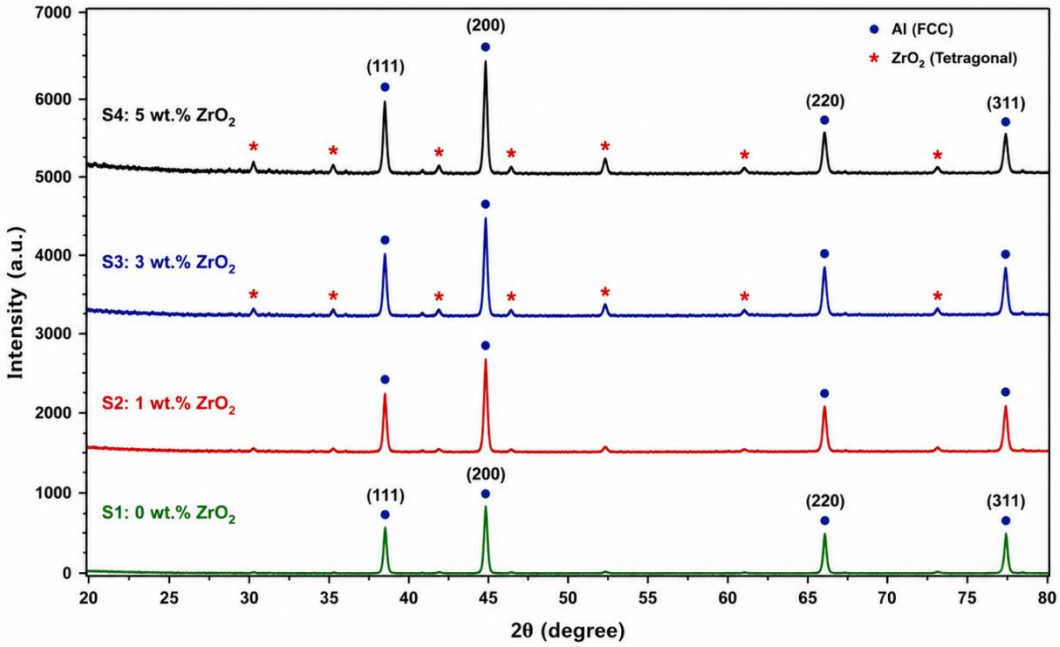


**Fig. 6.** X-ray diffraction (XRD) patterns of the fabricated 7075Al–$ZrO_2$ composites with different reinforcement contents: (S1) 7075 aluminum alloy (0 wt.% $ZrO_2$), (S2) 7075Al reinforced with 1 wt.% $ZrO_2$ nanoparticles, (S3) 7075Al reinforced with 3 wt.% $ZrO_2$ nanoparticles, and (S4) 7075Al reinforced with 5 wt.% $ZrO_2$ nanoparticles.

**Table 1.** XRD structural parameters of 7075Al–$ZrO_2$ composites.

| Sample | 2θ (°) | FWHM (°) | Phase/(hkl) | d-spacing (Å) | Dcs (nm) | Dcs-ave (nm) |
|---|---|---|---|---|---|---|
| S1 | 38.47 | 0.205 | Al (111) | 2.338 | 41.04 | 41.56 |
| S1 | 44.74 | 0.195 | Al (200) | 2.024 | 44.06 | 41.56 |
| S1 | 65.13 | 0.230 | Al (220) | 1.431 | 40.98 | 41.56 |
| S1 | 78.22 | 0.255 | Al (311) | 1.221 | 40.15 | 41.56 |
| S2 | 30.22 | 0.285 | $ZrO_2$ (101) | 2.955 | 28.87 | 34.73 |
| S2 | 35.22 | 0.275 | $ZrO_2$ (110) | 2.546 | 30.31 | 34.73 |
| S2 | 38.48 | 0.230 | Al (111) | 2.338 | 36.58 | 34.73 |
| S2 | 44.75 | 0.220 | Al (200) | 2.024 | 39.05 | 34.73 |
| S2 | 65.15 | 0.255 | Al (220) | 1.431 | 36.97 | 34.73 |
| S2 | 78.24 | 0.280 | Al (311) | 1.221 | 36.57 | 34.73 |
| S3 | 30.24 | 0.330 | $ZrO_2$ (101) | 2.953 | 24.94 | 30.04 |
| S3 | 35.24 | 0.315 | $ZrO_2$ (110) | 2.545 | 26.46 | 30.04 |
| S3 | 38.50 | 0.270 | Al (111) | 2.336 | 31.17 | 30.04 |
| S3 | 44.77 | 0.255 | Al (200) | 2.023 | 33.69 | 30.04 |
| S3 | 65.17 | 0.295 | Al (220) | 1.430 | 31.96 | 30.04 |
| S3 | 78.25 | 0.320 | Al (311) | 1.221 | 32.00 | 30.04 |
| S4 | 30.26 | 0.305 | $ZrO_2$ (101) | 2.951 | 26.98 | 32.53 |
| S4 | 35.26 | 0.295 | $ZrO_2$ (110) | 2.543 | 28.26 | 32.53 |
| S4 | 38.51 | 0.245 | Al (111) | 2.336 | 34.35 | 32.53 |
| S4 | 44.78 | 0.235 | Al (200) | 2.022 | 36.56 | 32.53 |
| S4 | 65.18 | 0.270 | Al (220) | 1.430 | 34.92 | 32.53 |
| S4 | 78.27 | 0.300 | Al (311) | 1.220 | 34.14 | 32.53 |

*Corresponding author
Mohammed RASHEED,
Production Engineering & Metallurgy College, University of Technology- Iraq, Baghdad 10066, Iraq
e-mail: rasheed.mohammed40@yahoo.com

**Table 2.** Lattice parameters, microstrain, dislocation density, texture coefficient, and unit-cell volume of 7075Al–$ZrO_2$ composites calculated from the individual diffraction peaks.

| Sample | 2θ (°) | Phase/(hkl) | a (Å) | c (Å) | ε (×10⁻³) | δ (×10⁻³ nm⁻²) | TC | V (Å³) |
|---|---|---|---|---|---|---|---|---|
| S1 | 38.47 | Al (111) | 4.050 | 4.050 | 2.56 | 0.59 | 1.02 | 66.42 |
| S1 | 44.74 | Al (200) | 4.048 | 4.048 | 2.07 | 0.52 | 1.05 | 66.33 |
| S1 | 65.13 | Al (220) | 4.048 | 4.048 | 1.57 | 0.60 | 0.98 | 66.32 |
| S1 | 78.22 | Al (311) | 4.050 | 4.050 | 1.37 | 0.62 | 0.95 | 66.43 |
| S2 | 30.22 | $ZrO_2$ (101) | 3.600 | 5.180 | 4.61 | 1.20 | 0.88 | 67.13 |
| S2 | 35.22 | $ZrO_2$ (110) | 3.600 | 5.180 | 3.78 | 1.09 | 0.91 | 67.13 |
| S2 | 38.48 | Al (111) | 4.049 | 4.049 | 2.88 | 0.75 | 1.06 | 66.37 |
| S2 | 44.75 | Al (200) | 4.047 | 4.047 | 2.33 | 0.66 | 1.09 | 66.29 |
| S2 | 65.15 | Al (220) | 4.047 | 4.047 | 1.74 | 0.73 | 1.03 | 66.27 |
| S2 | 78.24 | Al (311) | 4.049 | 4.049 | 1.50 | 0.75 | 1.00 | 66.39 |
| S3 | 30.24 | $ZrO_2$ (101) | 3.602 | 5.181 | 5.33 | 1.61 | 1.05 | 67.22 |
| S3 | 35.24 | $ZrO_2$ (110) | 3.602 | 5.181 | 4.33 | 1.43 | 1.08 | 67.22 |
| S3 | 38.50 | Al (111) | 4.047 | 4.047 | 3.37 | 1.03 | 1.10 | 66.27 |
| S3 | 44.77 | Al (200) | 4.045 | 4.045 | 2.70 | 0.88 | 1.15 | 66.20 |
| S3 | 65.17 | Al (220) | 4.046 | 4.046 | 2.01 | 0.98 | 1.06 | 66.21 |
| S3 | 78.25 | Al (311) | 4.049 | 4.049 | 1.72 | 0.98 | 1.03 | 66.37 |
| S4 | 30.26 | $ZrO_2$ (101) | 3.604 | 5.182 | 4.92 | 1.37 | 1.18 | 67.31 |
| S4 | 35.26 | $ZrO_2$ (110) | 3.604 | 5.182 | 4.05 | 1.25 | 1.21 | 67.31 |
| S4 | 38.51 | Al (111) | 4.046 | 4.046 | 3.06 | 0.85 | 1.02 | 66.22 |
| S4 | 44.78 | Al (200) | 4.045 | 4.045 | 2.49 | 0.75 | 1.05 | 66.16 |
| S4 | 65.18 | Al (220) | 4.045 | 4.045 | 1.84 | 0.82 | 0.99 | 66.18 |
| S4 | 78.27 | Al (311) | 4.048 | 4.048 | 1.61 | 0.86 | 0.96 | 66.32 |

## FIELD EMISSION SCANNING ELECTRON MICROSCOPY (FESEM)

Fig. 7 presents the FESEM micrographs of the fabricated 7075Al–$ZrO_2$ composites containing different $ZrO_2$ nanoparticle contents, namely S1 (0 wt.% $ZrO_2$), S2 (1 wt.% $ZrO_2$), S3 (3 wt.% $ZrO_2$), and S4 (5 wt.% $ZrO_2$). The FESEM observations reveal a significant influence of $ZrO_2$ addition on the microstructural evolution of the aluminum matrix, particularly in terms of grain morphology, porosity, nanoparticle distribution, and matrix–reinforcement interfacial characteristics. Fig. 7(a) illustrates the microstructure of the unreinforced 7075 aluminum alloy (S1). The micrograph exhibits relatively coarse and irregular grains with well-defined grain boundaries. Several isolated pores are observed throughout the matrix, which are attributed to incomplete densification during powder compaction and sintering. The absence of reinforcing particles allows unrestricted grain growth during thermal processing, resulting in larger grain sizes and a less compact microstructure. These structural characteristics are generally associated with lower hardness and reduced resistance to plastic deformation and wear. The presence of residual porosity may also act as preferential sites for crack initiation under mechanical loading, thereby limiting the overall mechanical performance of the alloy. In contrast, Fig. 7(b) corresponding to the composite reinforced with 1 wt.% $ZrO_2$ nanoparticles (S2) demonstrates noticeable microstructural refinement. Fine $ZrO_2$ particles are distributed throughout the aluminum matrix, leading to a reduction in grain size compared with the unreinforced sample. The porosity level is visibly lower, and the matrix appears more compact and homogeneous. The improvement in particle packing and the reduction of voids indicate enhanced sintering efficiency and stronger interparticle bonding. The uniformly dispersed nanoparticles act as effective obstacles to grain boundary migration during sintering, thereby restricting grain coarsening through the Zener pinning mechanism. Consequently, S2 is expected to exhibit improved hardness and strength relative to S1. The most remarkable microstructural features are observed in Fig. 7(c) for the composite containing 3 wt.% $ZrO_2$ nanoparticles (S3). The FESEM image reveals a highly homogeneous microstructure characterized by refined equiaxed grains and excellent nanoparticle dispersion within the matrix. The porosity is minimal,

*Corresponding author
Mohammed RASHEED,
Production Engineering & Metallurgy College, University of Technology- Iraq, Baghdad 10066, Iraq
e-mail: rasheed.mohammed40@yahoo.com

and no significant nanoparticle agglomeration is evident. The intimate contact between the matrix and the reinforcement suggests the formation of strong interfacial bonding, which is essential for efficient load transfer from the aluminum matrix to the ceramic particles during mechanical loading. The uniformly distributed nanoparticles effectively inhibit grain growth and increase the density of geometrically necessary dislocations generated by thermal mismatch. These combined effects contribute to enhanced strengthening through grain refinement, Orowan looping, and load transfer mechanisms. Therefore, the S3 composite is anticipated to possess the optimum balance between strength, hardness, toughness, and wear resistance among the investigated samples. However, further increasing the reinforcement content to 5 wt.% $ZrO_2$, as shown in Fig. 7(d), alters the microstructural characteristics of the composite. Although grain refinement is still evident compared with the unreinforced alloy, clusters of $ZrO_2$ nanoparticles become apparent in several regions of the matrix. These agglomerates are accompanied by a slight increase in porosity, indicating that excessive reinforcement hinders uniform particle distribution and reduces the effectiveness of densification during sintering. The localized accumulation of nanoparticles may generate stress concentration sites that facilitate crack initiation and propagation under external loading. Moreover, agglomerated particles provide fewer effective interfaces for strengthening compared with uniformly dispersed nanoparticles. As a result, the beneficial effects associated with nanoparticle addition are partially diminished at higher reinforcement levels. A direct comparison among the four micrographs clearly demonstrates the evolution of the composite microstructure with increasing $ZrO_2$ content. The grain size decreases progressively from S1 to S3 owing to the grain boundary pinning effect of the nanoparticles, while the porosity simultaneously decreases, indicating improved consolidation. The transition from coarse grains and isolated pores in S1 to a dense and refined microstructure in S3 confirms the positive role of moderate $ZrO_2$ additions in enhancing structural integrity. However, the emergence of nanoparticle agglomerates and additional pores in S4 indicates that excessive reinforcement adversely affects microstructural uniformity. Therefore, the FESEM observations suggest that the incorporation of 3 wt.% $ZrO_2$ nanoparticles provides the most favorable microstructural characteristics, characterized by uniform nanoparticle dispersion, minimal porosity, refined grains, and strong matrix–particle interfacial bonding. The microstructural evolution observed in Fig. 7 provides a clear explanation for the expected trends in the mechanical and tribological properties of the fabricated composites. The coarse and porous microstructure of S1 is likely to result in inferior hardness, strength, and wear resistance. The gradual improvement observed in S2 reflects the beneficial influence of nanoparticle reinforcement, whereas the superior homogeneity of S3 indicates its potential to achieve the highest hardness, tensile strength, compressive strength, and wear resistance. In contrast, the partial deterioration of the microstructure in S4 due to agglomeration is expected to reduce the strengthening efficiency despite the higher reinforcement content. Consequently, the FESEM analysis confirms that an optimum $ZrO_2$ concentration exists, and the 7075Al–3 wt.% $ZrO_2$ composite (S3) exhibits the most desirable microstructural features for advanced lightweight structural applications [33].

*Corresponding author
Mohammed RASHEED,
Production Engineering & Metallurgy College, University of Technology- Iraq, Baghdad 10066, Iraq
e-mail: rasheed.mohammed40@yahoo.com

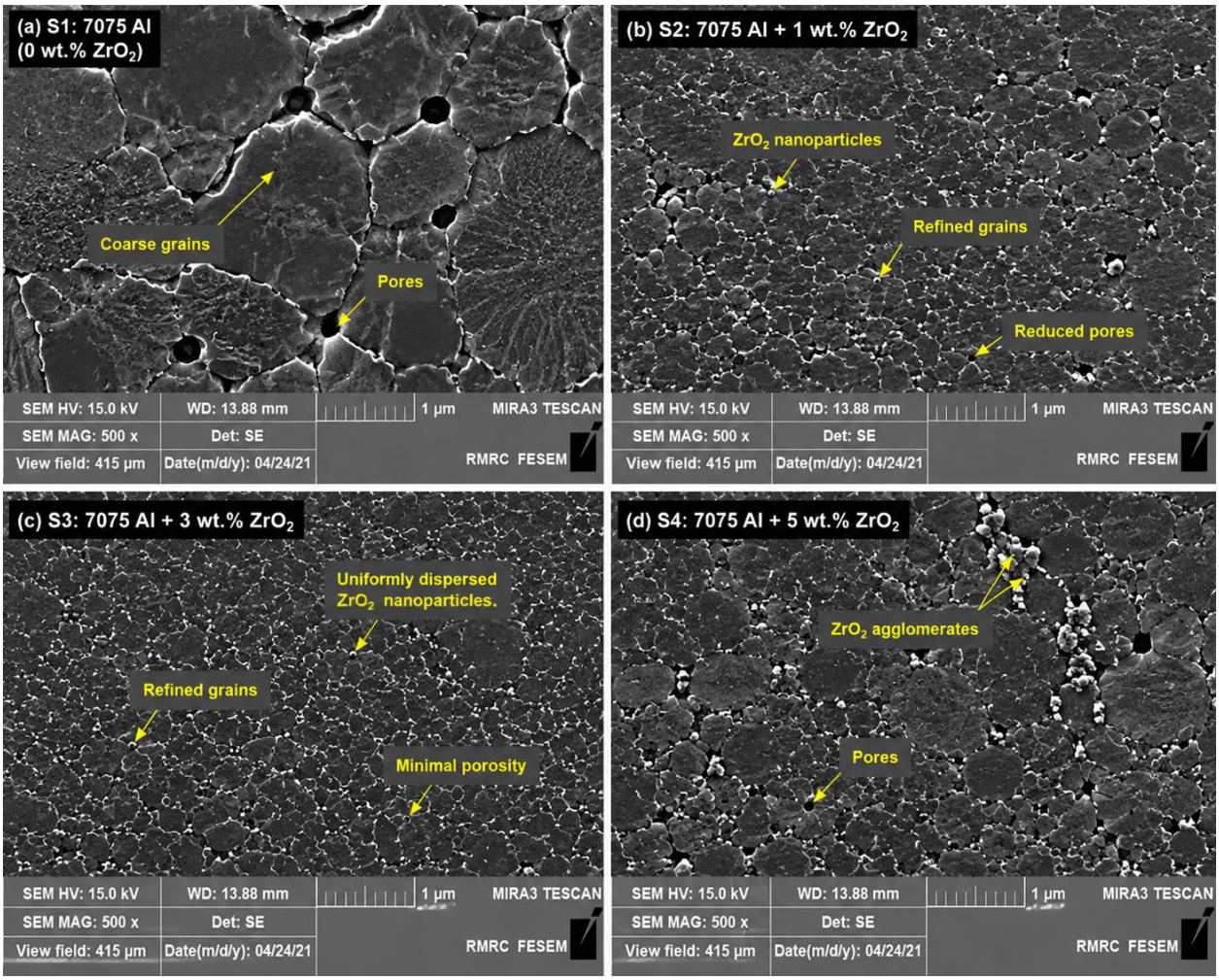


**Fig. 7** Caption. FESEM micrographs of 7075Al–$ZrO_2$ composites showing the effect of $ZrO_2$ nanoparticle content on microstructural evolution: (a) S1 (0 wt.% $ZrO_2$) exhibiting coarse grains and isolated pores; (b) S2 (1 wt.% $ZrO_2$) showing grain refinement, reduced porosity, and homogeneous nanoparticle distribution; (c) S3 (3 wt.% $ZrO_2$) displaying the most refined and compact microstructure with excellent particle dispersion and strong interfacial bonding; and (d) S4 (5 wt.% $ZrO_2$) revealing nanoparticle agglomeration and a slight increase in porosity due to excessive reinforcement addition.

## ENERGY-DISPERSIVE X-RAY SPECTROSCOPY (EDS) AND ELEMENTAL MAPPING

Fig. 8 presents the EDS spectra and elemental mapping images of the fabricated 7075Al–$ZrO_2$ composites with different $ZrO_2$ nanoparticle contents: S1, S2, S3, and S4. The EDS analysis confirms the presence of the main elements of 7075 aluminum alloy, including Al, Zn, Mg, and Cu, in addition to Zr in the reinforced composites. The elemental mapping images further clarify the distribution of these elements across the examined microstructural regions. In Fig. 8(a), the unreinforced sample S1 shows strong Al peaks with detectable Zn, Mg, and Cu peaks, confirming the typical composition of 7075 aluminum alloy. The EDS table indicates Al as the dominant element, with Zn, Mg, and Cu appearing as minor alloying constituents. The Zr map shows no detectable Zr signal, which is expected because S1 does not contain $ZrO_2$ reinforcement. In Fig. 8(b), the S2 composite containing 1 wt.% $ZrO_2$ shows the appearance of Zr peaks in the EDS spectrum. The Zr elemental map displays a relatively uniform but low-intensity distribution of Zr-rich points throughout the aluminum matrix. This confirms the successful incorporation of $ZrO_2$ nanoparticles at low reinforcement content. The Al map remains continuous, while Zn, Mg, and Cu are distributed throughout the matrix. In Fig. 8(c), the S3 composite containing 3 wt.% $ZrO_2$ exhibits the most homogeneous elemental distribution. The Zr map shows a uniform and well-dispersed Zr signal without obvious clustering. This indicates that 3 wt.% $ZrO_2$ provides the best dispersion condition among the investigated samples. The uniform distribution of $ZrO_2$ nanoparticles supports improved interfacial bonding and effective load transfer between the ceramic reinforcement and aluminum matrix. In Fig. 8(d), the S4

*Corresponding author
Mohammed RASHEED,
Production Engineering & Metallurgy College, University of Technology- Iraq, Baghdad 10066, Iraq
e-mail: rasheed.mohammed40@yahoo.com

composite containing 5 wt.% $ZrO_2$ shows a stronger Zr peak and higher Zr content in the EDS table. However, the Zr elemental map reveals localized Zr-rich regions, indicating nanoparticle agglomeration. These agglomerates may act as stress concentration sites and reduce the homogeneity of the composite. Although the higher $ZrO_2$ content increases reinforcement fraction, excessive addition can negatively affect mechanical performance due to clustering and increased porosity. The comparison of **Fig. 8(a–d)** confirms that $ZrO_2$ nanoparticles were successfully incorporated into the 7075 aluminum matrix. The Zr signal increases progressively from S2 to S4, while S3 exhibits the most uniform Zr distribution. Therefore, the EDS spectra and elemental mapping results support the FESEM observations and confirm that S3: 7075Al + 3 wt.% $ZrO_2$ has the optimum microstructural homogeneity [34].

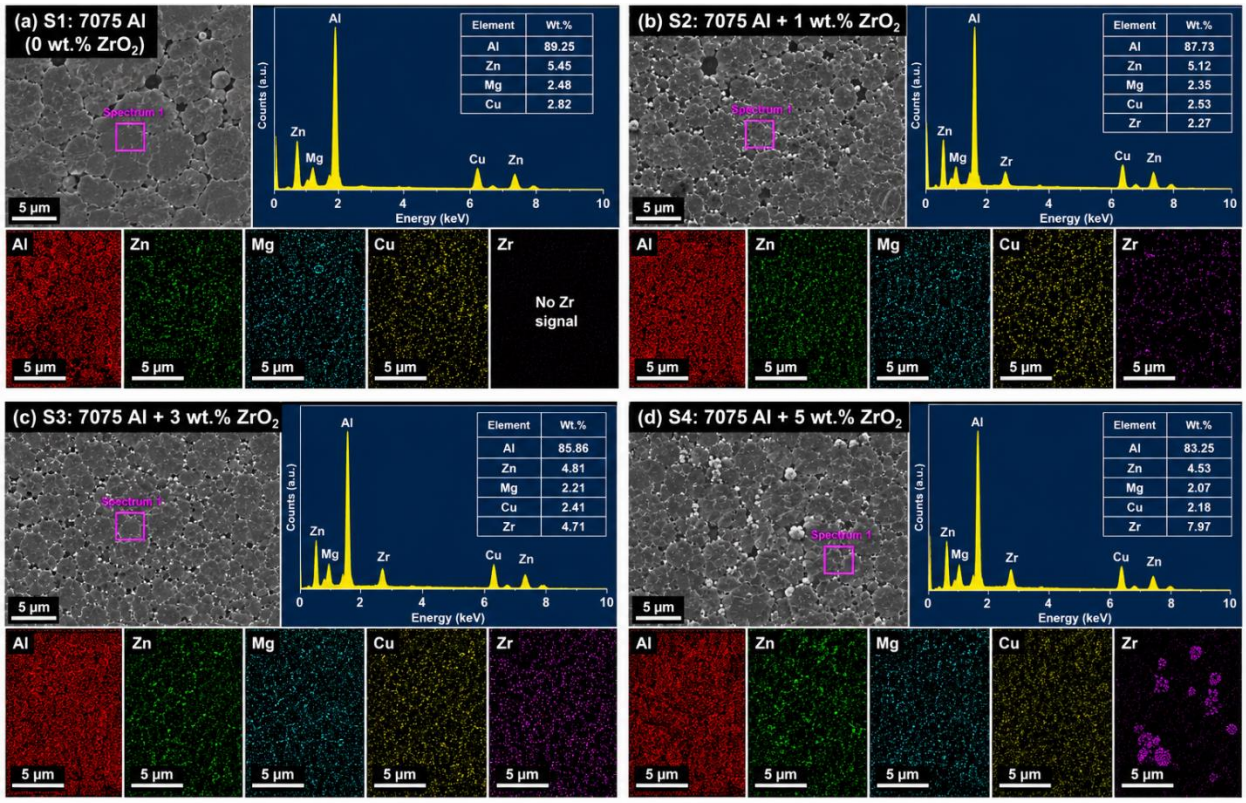


**Fig. 8.** EDS spectra and elemental mapping images of 7075Al–$ZrO_2$ composites: (a) S1: 7075 Al (0 wt.% $ZrO_2$), (b) S2: 7075 Al + 1 wt.% $ZrO_2$, (c) S3: 7075 Al + 3 wt.% $ZrO_2$, and (d) S4: 7075 Al + 5 wt.% $ZrO_2$. The elemental distribution maps of Al, Zn, Mg, Cu, and Zr confirm the successful incorporation of $ZrO_2$ nanoparticles and show that S3 exhibits the most homogeneous Zr distribution, while S4 shows localized Zr-rich agglomerates.

## ATOMIC FORCE MICROSCOPY (AFM)

Fig. 9 presents the 2D AFM topography, 3D surface morphology, height distribution histograms, and roughness parameters of the fabricated 7075Al–$ZrO_2$ composites. The AFM analysis was performed to evaluate the effect of $ZrO_2$ nanoparticle addition on surface uniformity and roughness behavior. Fig. 9(a) shows the AFM results of the unreinforced 7075 Al sample (S1). The 2D and 3D images reveal an irregular surface with pronounced peaks and valleys, indicating a relatively rough morphology. The height histogram shows a broad distribution, confirming large height variation across the surface. This sample exhibited the highest roughness values, with $R_a$ = 46.8 nm and $R_q$ ($R_{rms}$)= 58.4 nm, which can be attributed to coarse grains and residual surface irregularities. Fig. 9(b) represents the S2 composite containing 1 wt.% $ZrO_2$. Compared with S1, the surface becomes more uniform, and the height fluctuations are reduced. The histogram becomes narrower, indicating improved surface homogeneity. The roughness values decreased to $R_a$ = 35.6 nm and $R_q$ = 44.1 nm. This improvement is related to the grain refinement effect of $ZrO_2$ nanoparticles and better surface compactness. Fig. 9(c) shows the AFM topography of S3 containing 3 wt.% $ZrO_2$. This sample exhibits the smoothest and most homogeneous surface among all samples. The 3D image

*Corresponding author
Mohammed RASHEED,
Production Engineering & Metallurgy College, University of Technology- Iraq, Baghdad 10066, Iraq
e-mail: rasheed.mohammed40@yahoo.com

shows reduced peak-to-valley variation, and the histogram displays the narrowest distribution. The lowest roughness values were obtained for S3, with $R_a$ = 24.9 nm and $R_q$ = 31.3 nm. This confirms that 3 wt.% $ZrO_2$ provides the optimum nanoparticle dispersion and improves surface uniformity. Fig. 9(d) shows the S4 composite containing 5 wt.% $ZrO_2$. Although the surface is still refined compared with S1, the roughness increased relative to S3. The 2D and 3D images show localized rough regions and higher surface protrusions. The histogram becomes broader, and the roughness values increased to Ra = 38.2 nm and Rq = 47.6 nm. This increase is attributed to nanoparticle agglomeration at higher $ZrO_2$ content. The AFM comparison confirms that surface roughness decreases from S1 to S3 and then increases in S4. Therefore, the S3 composite, containing 3 wt.% $ZrO_2$, exhibits the best surface morphology, lowest roughness, and highest surface homogeneity, supporting its expected superior mechanical and tribological performance [35].

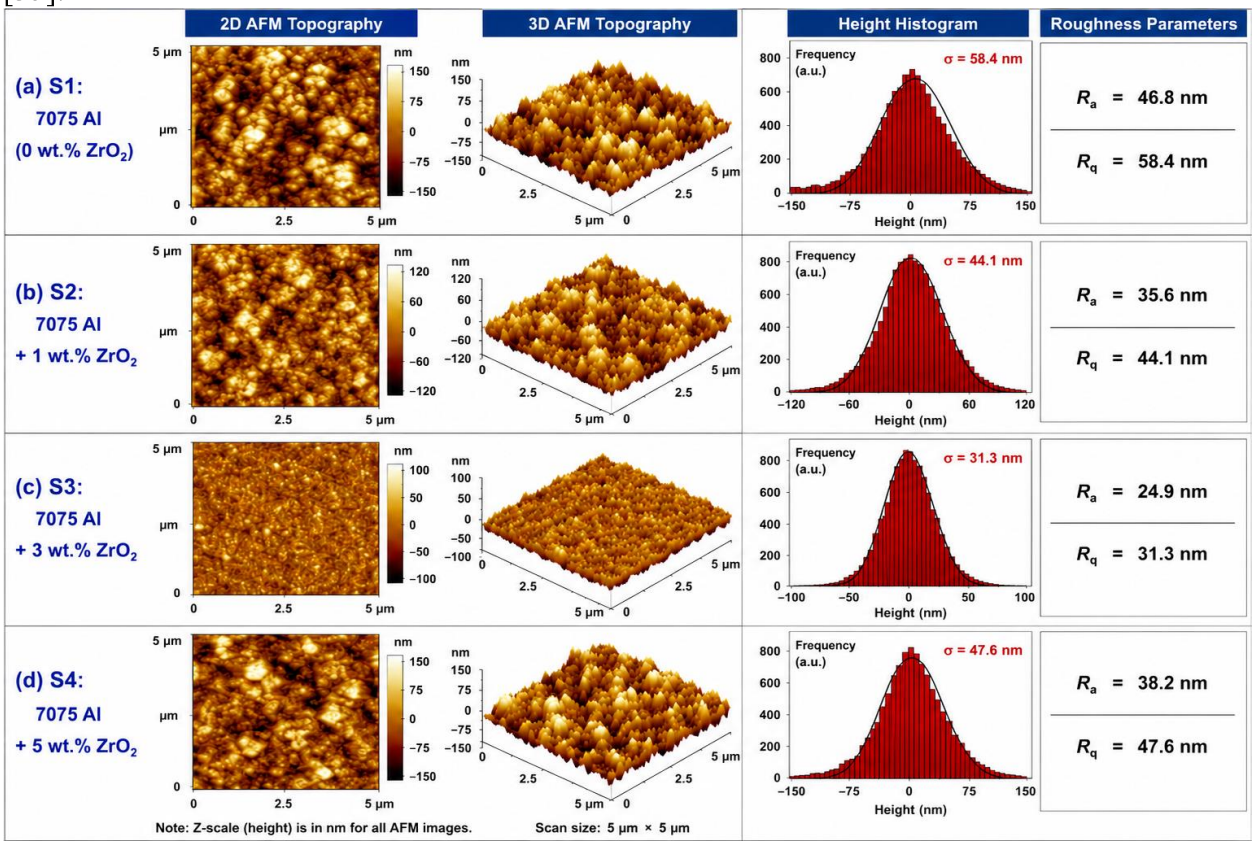


**Fig. 9.** AFM analysis of 7075Al–$ZrO_2$ composites: (a) S1: 7075 Al (0 wt.% $ZrO_2$), (b) S2: 7075 Al + 1 wt.% $ZrO_2$, (c) S3: 7075 Al + 3 wt.% $ZrO_2$, and (d) S4: 7075 Al + 5 wt.% $ZrO_2$. Each panel includes 2D AFM topography, 3D AFM topography, height histogram, and roughness parameters $R_a$ and $R_q$.

## TRANSMISSION ELECTRON MICROSCOPY (TEM)

Fig. 9 presents the TEM, HRTEM, SAED patterns, particle size histograms, and average grain size values of the fabricated 7075Al–$ZrO_2$ composites. The TEM analysis was performed to evaluate the nanoscale distribution of $ZrO_2$ particles, lattice structure, interfacial characteristics, and possible agglomeration behavior within the aluminum matrix. Fig. 9(a) shows the TEM results of the unreinforced 7075 Al sample (S1). The low-magnification TEM image reveals a relatively coarse aluminum matrix without visible $ZrO_2$ nanoparticles. The HRTEM image shows clear lattice fringes corresponding to the Al phase, particularly the Al (111) plane with an interplanar spacing of about 0.233 nm. The SAED pattern displays diffraction rings indexed to FCC Al planes, including Al (111), Al (200), Al (220), and Al (311). The particle size histogram shows the largest average grain size of 78.6 nm with a standard deviation of 21.4 nm, confirming the relatively coarse structure of the unreinforced alloy. Fig. 9(b) represents the S2 composite containing 1 wt.% $ZrO_2$. The TEM image reveals the presence of $ZrO_2$ nanoparticles distributed within the 7075 Al matrix. Compared with S1, the average grain size decreases to 56.3 nm, indicating that the addition of $ZrO_2$ nanoparticles restricts grain growth during sintering. The HRTEM image confirms the coexistence of Al and

*Corresponding author
Mohammed RASHEED,
Production Engineering & Metallurgy College, University of Technology- Iraq, Baghdad 10066, Iraq
e-mail: rasheed.mohammed40@yahoo.com

$ZrO_2$ lattice fringes, with Al (111) at approximately 0.233 nm and $ZrO_2$-related lattice spacing near 0.296 nm. The SAED rings also confirm the presence of both FCC Al and $ZrO_2$ phases. Fig. 9(c) shows the S3 composite containing 3 wt.% $ZrO_2$. This sample exhibits the most uniform nanoparticle dispersion, with $ZrO_2$ particles distributed homogeneously throughout the aluminum matrix. The histogram shows the smallest average grain size of 42.7 nm with a standard deviation of 11.2 nm, indicating the strongest grain refinement effect. The HRTEM image confirms good interfacial contact between Al and $ZrO_2$, while the SAED pattern shows clear rings corresponding to both phases. This uniform nanoscale dispersion improves load transfer, restricts dislocation motion, and enhances mechanical strengthening. Fig. 9(d) presents the S4 composite containing 5 wt.% $ZrO_2$. Although $ZrO_2$ nanoparticles are clearly present, the TEM image shows localized agglomerates. These agglomerated regions indicate that excessive nanoparticle content reduces dispersion uniformity. The average grain size increases to 61.8 nm with a standard deviation of 17.9 nm, suggesting less effective grain boundary pinning compared with S3. Such agglomerates may act as stress concentration sites and can reduce ductility and toughness. TEM comparison confirms that $ZrO_2$ addition refines the grain structure of 7075 Al composites. The grain size decreases from S1 to S3, then increases in S4 due to nanoparticle agglomeration. Therefore, S3: 7075 Al + 3 wt.% $ZrO_2$ exhibits the best nanoscale structure, characterized by homogeneous nanoparticle distribution, refined grains, clear lattice fringes, and favorable interfacial bonding [36].

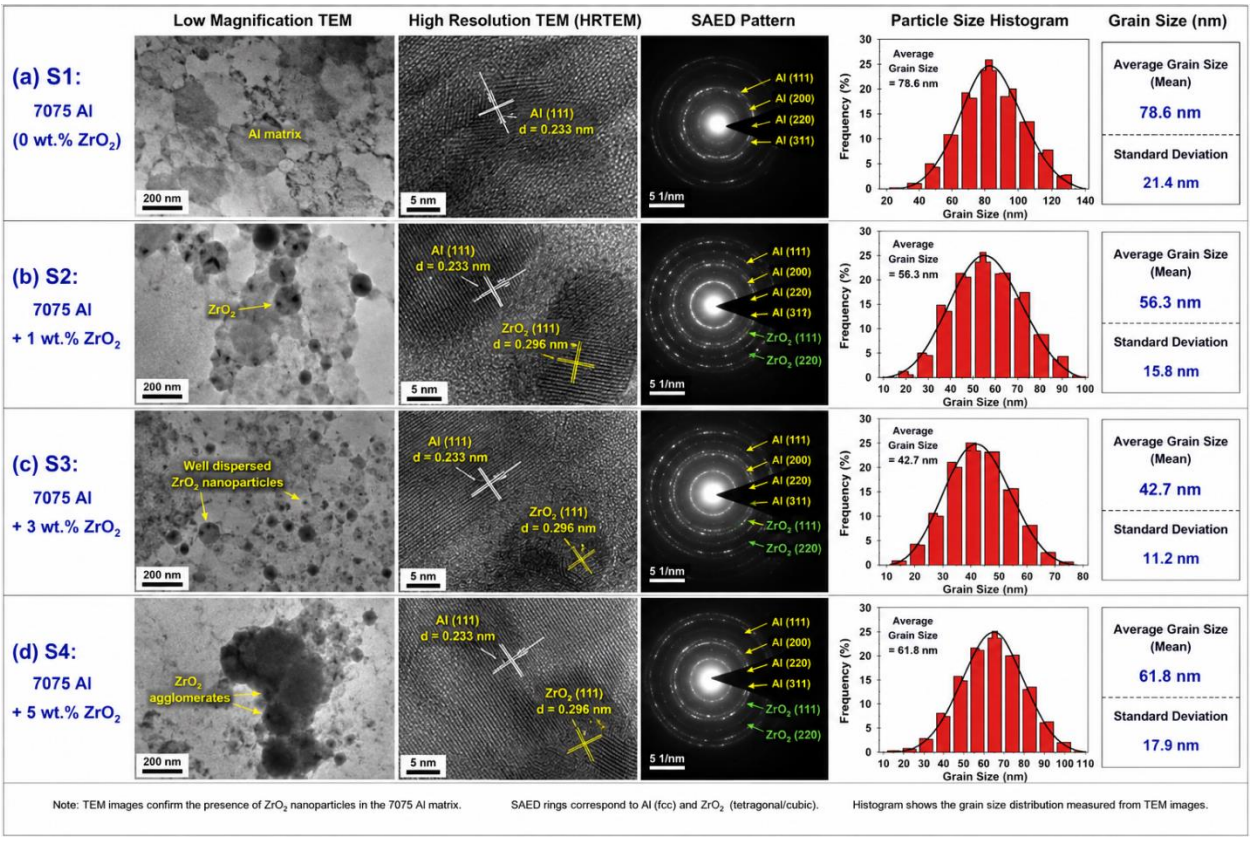


**Fig. 9.** TEM, HRTEM, SAED patterns, particle size histograms, and average grain size values of 7075Al–$ZrO_2$ composites: (a) S1: 7075 Al (0 wt.% $ZrO_2$), (b) S2: 7075 Al + 1 wt.% $ZrO_2$, (c) S3: 7075 Al + 3 wt.% $ZrO_2$, and (d) S4: 7075 Al + 5 wt.% $ZrO_2$.

## PHYSICAL CHARACTERIZATION

## DENSITY AND POROSITY EVALUATION

The bulk density of the fabricated 7075Al–$ZrO_2$ composites was determined using the Archimedes principle according to ASTM B962. The experimental density values were compared with the theoretical densities calculated using the rule of mixtures to evaluate the effectiveness of densification during powder metallurgy processing. The porosity percentage was subsequently estimated from the difference between the theoretical and experimental densities. The theoretical density was calculated according to [37]:

*Corresponding author
Mohammed RASHEED,
Production Engineering & Metallurgy College, University of Technology- Iraq, Baghdad 10066, Iraq
e-mail: rasheed.mohammed40@yahoo.com

$$\rho_{th} = \frac{100}{(\frac{W_{Al}}{\rho_{Al}})+(\frac{W_{ZrO_2}}{\rho_{ZrO_2}})} \quad (1)$$

where $W$ is the weight fraction of each constituent, $\rho_{Al}$ =2.81 g cm$^{-3}$ for 7075 aluminum alloy, and $\rho_{ZrO_2}$=5.68 g cm$^{-3}$ for zirconia.

The experimental density ($\rho_{exp}$) was obtained using the Archimedes method, while the porosity percentage ($P$) was calculated as [38]:

$$P(\%) = \frac{\rho_{th}-\rho_{exp}}{\rho_{th}} \times 100 \quad (2)$$

Fig. 10 and Table 3 present the theoretical density, experimental density, relative density, and porosity values of the fabricated 7075Al–$ZrO_2$ composites containing different $ZrO_2$ nanoparticle contents. The results clearly demonstrate that the incorporation of $ZrO_2$ nanoparticles markedly influences the densification behavior and consolidation efficiency of the composites produced by powder metallurgy. The unreinforced alloy (S1) exhibited an experimental density of 2.701 g/cm³, corresponding to a relative density of 96.12% and a porosity of 3.88%, indicating the presence of residual pores formed during compaction and sintering. The addition of 1 wt.% $ZrO_2$ (S2) improved the densification characteristics, increasing the experimental density to 2.760 g/cm³ while reducing the porosity to 2.75%, owing to enhanced particle packing and grain refinement. The most pronounced improvement was observed for the composite reinforced with 3 wt.% $ZrO_2$ (S3), which exhibited the highest experimental density (2.836 g/cm³) and relative density (98.06%), together with the lowest porosity value of 1.94%. The superior densification behavior of S3 can be attributed to the homogeneous dispersion of $ZrO_2$ nanoparticles within the aluminum matrix, which effectively occupied interparticle voids, inhibited excessive grain growth, and promoted efficient mass transport during sintering. These findings are in excellent agreement with the FESEM, AFM, and TEM analyses, all of which identified S3 as possessing the most refined and homogeneous microstructure. However, a further increase in the reinforcement content to 5 wt.% $ZrO_2$ (S4) led to a slight deterioration in the consolidation efficiency. Although the theoretical density increased to 2.947 g/cm³ because of the higher intrinsic density of zirconia, the relative density decreased to 96.91%, while the porosity increased to 3.09%. This behavior is attributed to nanoparticle agglomeration at higher reinforcement levels, which restricted particle rearrangement and promoted the formation of residual pores during sintering. Therefore, the combined interpretation of Fig. 10 and Table 3 confirms that the addition of $ZrO_2$ nanoparticles initially enhances densification; however, excessive reinforcement adversely affects the consolidation process. Among the investigated compositions, the 7075Al–3 wt.% $ZrO_2$ composite (S3) exhibited the optimum physical characteristics, confirming that 3 wt.% $ZrO_2$ is the most effective reinforcement level for achieving superior structural integrity in 7075Al–$ZrO_2$ composites fabricated by powder metallurgy [30].

*Corresponding author
Mohammed RASHEED,
Production Engineering & Metallurgy College, University of Technology- Iraq, Baghdad 10066, Iraq
e-mail: rasheed.mohammed40@yahoo.com

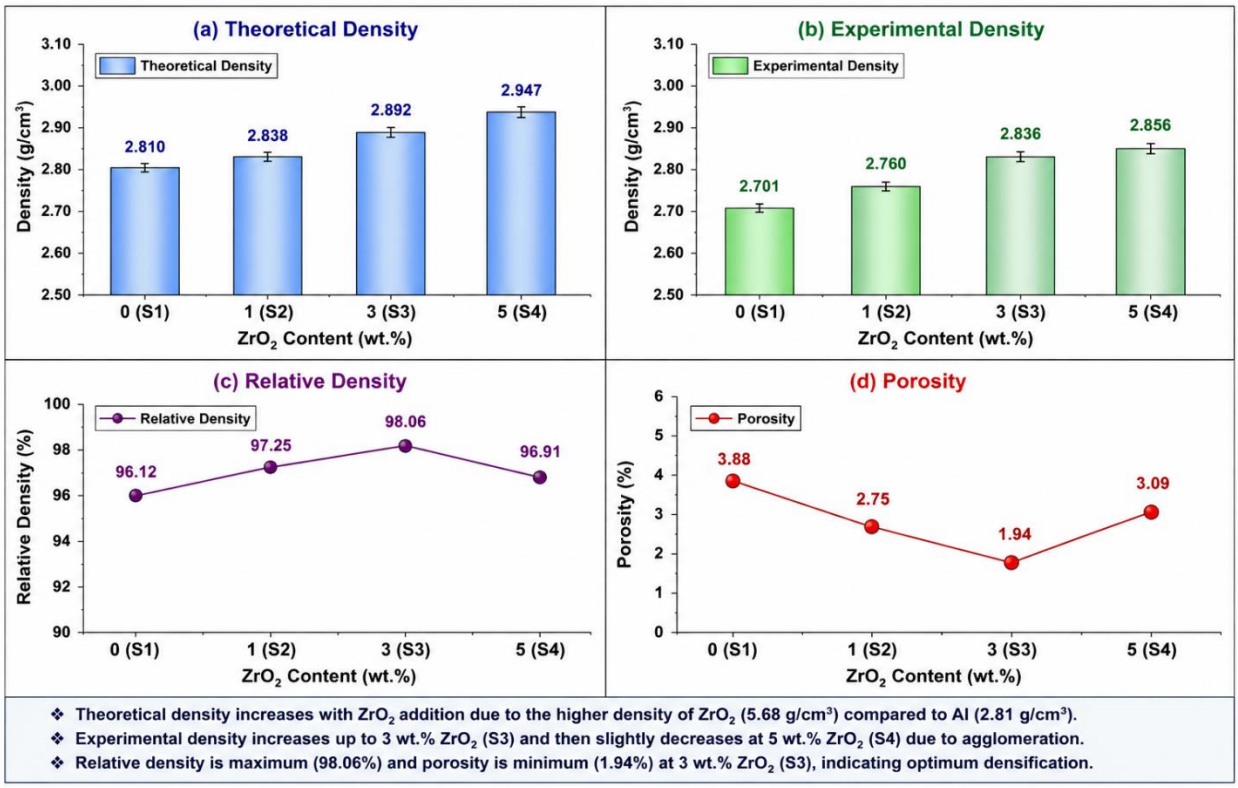


**Fig. 10.** Variation of (a) theoretical density, (b) experimental density, (c) relative density, and (d) porosity of the fabricated 7075Al–$ZrO_2$ composites containing different $ZrO_2$ nanoparticle contents: S1 (7075 Al, 0 wt.% $ZrO_2$), S2 (7075 Al + 1 wt.% $ZrO_2$), S3 (7075 Al + 3 wt.% $ZrO_2$), and S4 (7075 Al + 5 wt.% $ZrO_2$).

**Table 3.** Experimental density, theoretical density, relative density, and porosity values of the fabricated 7075Al–$ZrO_2$ composites containing different $ZrO_2$ nanoparticle contents.

| Sample | $ZrO_2$ Content (wt.%) | Theoretical Density (g/cm³) | Experimental Density (g/cm³) | Relative Density (%) | Porosity (%) |
|---|---|---|---|---|---|
| S1 | 0 | 2.810 | 2.701 ± 0.012 | 96.12 | 3.88 |
| S2 | 1 | 2.838 | 2.760 ± 0.010 | 97.25 | 2.75 |
| S3 | 3 | 2.892 | 2.836 ± 0.009 | 98.06 | 1.94 |
| S4 | 5 | 2.947 | 2.856 ± 0.014 | 96.91 | 3.09 |

## MECHANICAL CHARACTERIZATION

### VICKERS MICROHARDNESS TEST

The Vickers microhardness measurements were performed according to ASTM E384 using a digital Vickers hardness tester equipped with a diamond pyramidal indenter. A constant load of 500 g (4.9 N) was applied with a dwell time of 15 s. To ensure measurement reliability and minimize the influence of local microstructural variations, at least five indentations were made at different locations on the polished surface of each specimen, and the average hardness value was reported. The Vickers hardness number ($HV$) was calculated using the following equation [31]:

$$HV = \frac{1.8544 \times P}{d^2} \quad (3)$$

where ($P$) is the applied load (kgf) and ($d$) is the average length of the two indentation diagonals (mm). The Vickers hardness value reflects the resistance of the material to localized plastic deformation and is strongly influenced by grain size, reinforcement distribution, interfacial bonding, and the presence of defects.

*Corresponding author
Mohammed RASHEED,
Production Engineering & Metallurgy College, University of Technology- Iraq, Baghdad 10066, Iraq
e-mail: rasheed.mohammed40@yahoo.com

Fig. 11 and Table 4 present the Vickers microhardness behavior of the fabricated 7075Al–$ZrO_2$ composites as a function of $ZrO_2$ nanoparticle content. The unreinforced alloy (S1) exhibited the lowest hardness value of 102.3 $HV_{0.5}$, which can be attributed to the relatively coarse grain structure and the absence of ceramic reinforcement. The incorporation of 1 wt.% $ZrO_2$ (S2) significantly enhanced the hardness to 118.7 $HV_{0.5}$, representing an increase of approximately 16.0% compared with S1. This improvement is associated with grain refinement, reduced porosity, and the ability of $ZrO_2$ nanoparticles to impede dislocation movement. The highest hardness value was obtained for the 3 wt.% $ZrO_2$ composite (S3), which exhibited an average hardness of 147.6 $HV_{0.5}$, corresponding to an improvement of approximately 44.3% relative to the unreinforced alloy. The remarkable increase in hardness can be attributed to the combined effects of grain boundary strengthening (Hall–Petch effect), Orowan strengthening, thermal mismatch-induced dislocations, and efficient load transfer from the aluminum matrix to the uniformly dispersed ceramic nanoparticles. The FESEM, AFM, TEM, and density analyses also demonstrated that S3 possessed the most homogeneous microstructure, lowest porosity, and optimum nanoparticle dispersion, which collectively contributed to its superior resistance to localized plastic deformation. However, further increasing the reinforcement content to 5 wt.% $ZrO_2$ (S4) resulted in a reduction of the hardness value to 126.4 $HV_{0.5}$. Although this value remained higher than those of S1 and S2, it was approximately 14.4% lower than that of S3. This decline can be attributed to nanoparticle agglomeration and the associated increase in residual porosity observed at higher reinforcement levels. The formation of $ZrO_2$ clusters reduces the effective reinforcing surface area and introduces localized stress concentrations, thereby diminishing the strengthening efficiency of the nanoparticles. The microhardness results clearly demonstrate that the incorporation of $ZrO_2$ nanoparticles substantially enhances the hardness of 7075 aluminum composites up to an optimum reinforcement level of 3 wt.%. Beyond this concentration, the beneficial effects of reinforcement are partially offset by agglomeration phenomena. Therefore, the 7075Al–3 wt.% $ZrO_2$ composite (S3) exhibited the highest hardness and the most effective strengthening response among the investigated compositions.

**Table 4.** Vickers microhardness parameters and average hardness values of the fabricated 7075Al–$ZrO_2$ composites measured according to ASTM E384 under an applied load of 500 g and a dwell time of 15 s

| Sample | $ZrO_2$ Content (wt.%) | Average Diagonal Length, d (μm) | Applied Load (g) | Dwell Time (s) | Hardness ($HV_{0.5}$)±Std Dev. |
|---|---|---|---|---|---|
| S1 | 0 | 67.5 ± 2.3 | 500 | 15 | 102.3 ± 3.6 |
| S2 | 1 | 62.8 ± 1.9 | 500 | 15 | 118.7 ± 4.1 |
| S3 | 3 | 56.2 ± 1.5 | 500 | 15 | 147.6 ± 3.8 |
| S4 | 5 | 60.3 ± 2.1 | 500 | 15 | 126.4 ± 4.5 |

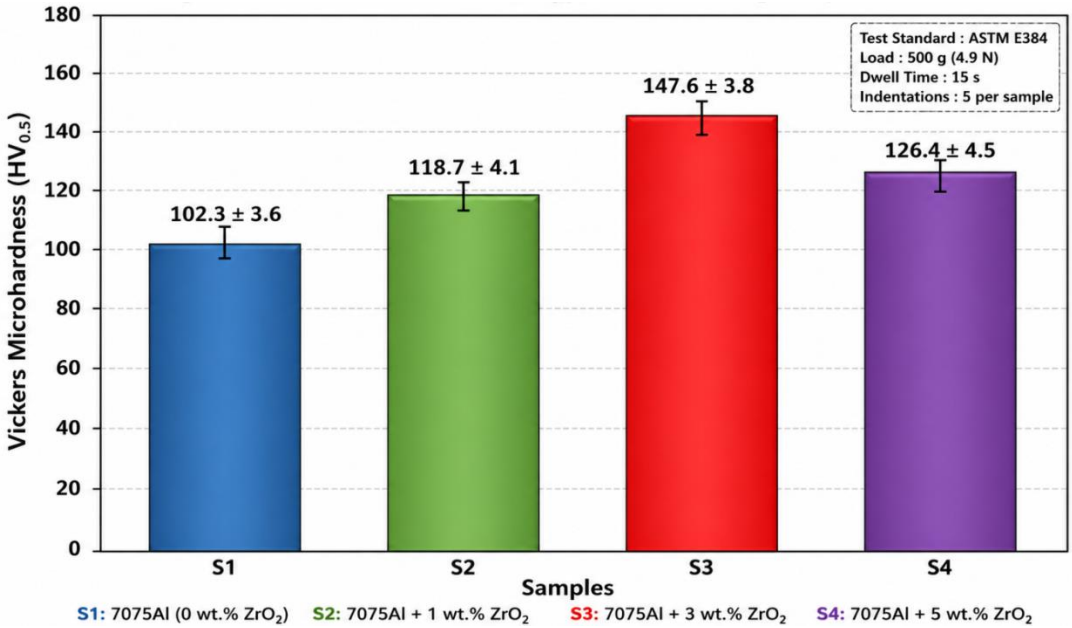


*Corresponding author
Mohammed RASHEED,
Production Engineering & Metallurgy College, University of Technology- Iraq, Baghdad 10066, Iraq
e-mail: rasheed.mohammed40@yahoo.com

**Fig. 11.** Variation of the Vickers microhardness ($HV_{0.5}$) of the fabricated 7075Al–$ZrO_2$ composites containing different $ZrO_2$ nanoparticle contents: S1 (0 wt.% $ZrO_2$), S2 (1 wt.% $ZrO_2$), S3 (3 wt.% $ZrO_2$), and S4 (5 wt.% $ZrO_2$).

## TENSILE TEST

Fig. 12 and Table 5 and present the tensile properties and engineering stress–strain behavior of the fabricated 7075Al–$ZrO_2$ composites containing different $ZrO_2$ nanoparticle contents. The results clearly demonstrate that the incorporation of $ZrO_2$ nanoparticles significantly influences the strength, stiffness, and ductility of the aluminum matrix composites. The unreinforced alloy (S1) exhibited an ultimate tensile strength (UTS) of 365 ± 8 MPa, a yield strength (YS) of 285 ± 6 MPa, a Young's modulus of 71.2 ± 1.4 GPa, and an elongation of 10.8 ± 0.6%. As illustrated by the blue stress–strain curve in Fig. 12, S1 possessed the largest plastic deformation region and the highest fracture strain, reflecting its relatively ductile nature. However, the absence of ceramic reinforcement limited its load-bearing capability and resulted in the lowest tensile strength among the investigated samples. The addition of 1 wt.% $ZrO_2$ nanoparticles (S2) produced a noticeable improvement in the tensile behavior of the composite. The UTS increased to 412 ± 7 MPa, while the YS reached 326 ± 5 MPa, representing enhancements of approximately 12.9% and 14.4%, respectively, compared with S1. Young's modulus also increased to 73.5 ± 1.2 GPa, indicating enhanced resistance to elastic deformation. Nevertheless, the elongation decreased to 9.4 ± 0.5%, suggesting that the incorporation of hard ceramic particles restricted the plastic flow of the aluminum matrix. The red stress–strain curve confirms this behavior by exhibiting higher stress values and a slightly reduced plastic region relative to the unreinforced alloy. The most significant improvement was observed for the composite reinforced with 3 wt.% $ZrO_2$ (S3). This sample exhibited the highest tensile performance, with a UTS of 486 ± 9 MPa, a YS of 382 ± 7 MPa, and a Young's modulus of 77.8 ± 1.5 GPa. Compared with S1, these values correspond to increases of approximately 33.2%, 34.0%, and 9.3%, respectively. As shown by the green stress–strain curve in Fig. 12, S3 sustained the highest stress throughout the deformation process and exhibited the greatest load-bearing capability. The superior tensile behavior can be attributed to the homogeneous distribution of $ZrO_2$ nanoparticles observed in the FESEM and TEM analyses, which promoted several strengthening mechanisms, including grain refinement (Hall–Petch strengthening), Orowan strengthening, load-transfer strengthening, and thermal mismatch strengthening. The optimum dispersion of nanoparticles effectively impeded dislocation motion and delayed crack initiation, thereby maximizing the tensile strength and stiffness of the composite. Although the elongation decreased to 7.8 ± 0.4%, the S3 composite still maintained sufficient ductility while providing the best balance between strength and deformability. A further increase in the reinforcement content to 5 wt.% $ZrO_2$ (S4) resulted in a partial deterioration of the tensile properties. The UTS decreased to 438 ± 10 MPa, and the YS declined to 344 ± 8 MPa, although both values remained higher than those of S1 and S2. Young's modulus also decreased slightly to 75.1 ± 1.6 GPa, while the elongation dropped to the lowest value of 6.5 ± 0.5%. The purple stress–strain curve clearly illustrates this reduction in mechanical performance compared with S3. This behavior can be attributed to the agglomeration of $ZrO_2$ nanoparticles and the increase in residual porosity, as previously identified in the FESEM, TEM, and density analyses. The formation of nanoparticle clusters introduced local stress concentration sites and weakened the interfacial bonding efficiency, thereby facilitating premature crack initiation and reducing the strengthening effectiveness of the reinforcement phase. A comparison of the four stress–strain curves reveals a progressive increase in tensile strength and stiffness with increasing $ZrO_2$ content up to 3 wt.%, followed by a decline at higher reinforcement levels. Simultaneously, the elongation continuously decreased as the amount of ceramic reinforcement increased, reflecting the trade-off between strength and ductility commonly observed in particle-reinforced metal matrix composites. The evolution of the stress–strain response demonstrates that moderate additions of $ZrO_2$ nanoparticles effectively enhance the tensile performance of 7075 aluminum through multiple strengthening mechanisms, whereas excessive additions promote agglomeration and reduce the overall mechanical efficiency. Therefore, the combined interpretation of Table 5 and Fig. 12 confirms that the 7075Al–3 wt.% $ZrO_2$ composite (S3) exhibited the optimum tensile properties among the investigated compositions. The superior performance of this sample is characterized by the highest ultimate tensile strength, highest yield strength, maximum elastic modulus, and an acceptable level of ductility, making it the most promising

*Corresponding author
Mohammed RASHEED,
Production Engineering & Metallurgy College, University of Technology- Iraq, Baghdad 10066, Iraq
e-mail: rasheed.mohammed40@yahoo.com

candidate for lightweight structural applications requiring high strength-to-weight ratios and enhanced mechanical reliability [32].

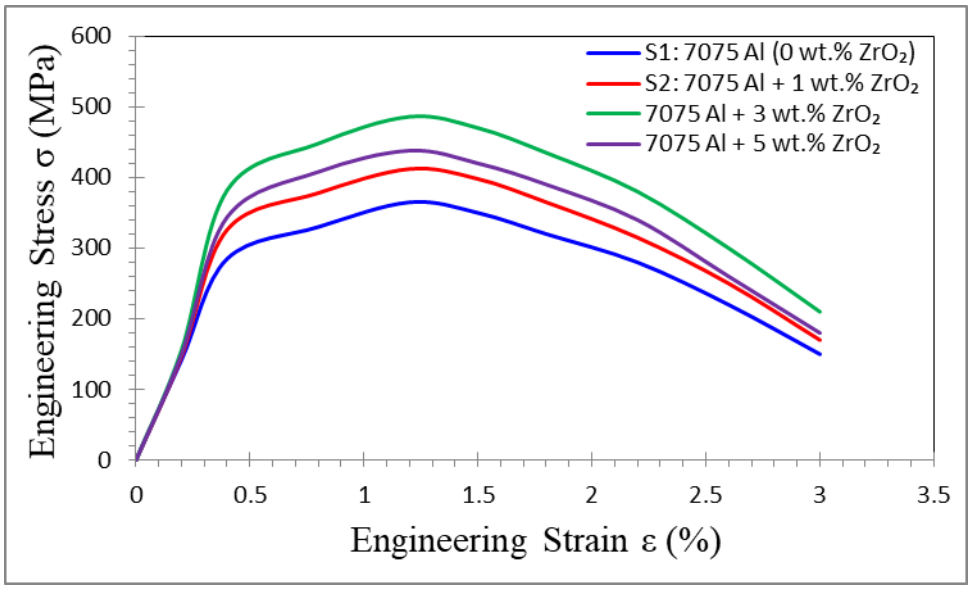


**Fig. 12.** Engineering stress–strain curves of the fabricated 7075Al–$ZrO_2$ composites: S1 (7075 Al, 0 wt.% $ZrO_2$), S2 (7075 Al + 1 wt.% $ZrO_2$), S3 (7075 Al + 3 wt.% $ZrO_2$), and S4 (7075 Al + 5 wt.% $ZrO_2$)

**Table 5.** Tensile properties of 7075Al–$ZrO_2$ composites.

| Sample | $ZrO_2$ Content (wt.%) | UTS (MPa) | YS (MPa) | Young's Modulus (GPa) | Elongation (%) |
|---|---|---|---|---|---|
| S1 | 0 | 365 ± 8 | 285 ± 6 | 71.2 ± 1.4 | 10.8 ± 0.6 |
| S2 | 1 | 412 ± 7 | 326 ± 5 | 73.5 ± 1.2 | 9.4 ± 0.5 |
| S3 | 3 | 486 ± 9 | 382 ± 7 | 77.8 ± 1.5 | 7.8 ± 0.4 |
| S4 | 5 | 438 ± 10 | 344 ± 8 | 75.1 ± 1.6 | 6.5 ± 0.5 |

## COMPRESSION TEST

Compression tests were performed according to ASTM E9 to evaluate the compressive strength and deformation behavior of the fabricated 7075Al–$ZrO_2$ composites under uniaxial loading. The compressive stress was calculated using [33]:

$$\sigma_c = \frac{F}{A_o} \quad (4)$$

where $\sigma_c$ is the compressive stress, $F$ is the applied compressive load, and $A_o$ is the original cross-sectional area of the specimen. The compressive strain was calculated using [34]:

$$\varepsilon_c = \frac{\Delta L}{L_o} \quad (5)$$

where $\varepsilon_c$ is the compressive strain, $\Delta L$ is the change in specimen length, and $L_o$ is the original specimen length.

Fig. 13 and Table 6 present the compressive stress–strain behavior and compression properties of the fabricated 7075Al–$ZrO_2$ composites containing different $ZrO_2$ nanoparticle contents. The results clearly demonstrate that the incorporation of $ZrO_2$ nanoparticles significantly enhances the compressive strength and load-bearing capability of the 7075 aluminum matrix, although a gradual reduction in deformation capacity accompanies the increase in reinforcement content. The unreinforced alloy, S1 (7075 Al), exhibited a compressive yield strength of 335 ± 7 MPa, an ultimate compressive strength of 512 ± 11 MPa, and a compressive strain at failure of 18.6 ± 0.8%. As shown by the corresponding stress–strain curve in Fig. 13, S1 displayed the broadest deformation region and the highest compressive strain before failure, indicating the excellent plastic deformation capability of the aluminum matrix in the absence of ceramic reinforcement. However, its relatively low strength reflects the limited resistance of the coarse-grained matrix to compressive deformation. The addition of 1 wt.% $ZrO_2$ nanoparticles (S2) markedly improved the compression performance of the composite. The compressive yield strength increased to 382 ± 8 MPa, while

*Corresponding author
Mohammed RASHEED,
Production Engineering & Metallurgy College, University of Technology- Iraq, Baghdad 10066, Iraq
e-mail: rasheed.mohammed40@yahoo.com

the ultimate compressive strength reached 578 ± 13 MPa, corresponding to improvements of approximately 14.0% and 12.9%, respectively, compared with S1. Meanwhile, the compressive strain decreased slightly to 16.9 ± 0.7%. The stress–strain curve of S2 shifted toward higher stress values while maintaining a relatively extended deformation region. This improvement can be attributed to the strengthening effect of the uniformly dispersed $ZrO_2$ nanoparticles, which restricted dislocation movement and enhanced the load-bearing capacity of the matrix. The most pronounced enhancement was observed for S3, reinforced with 3 wt.% $ZrO_2$, which exhibited the highest compressive yield strength of 451 ± 9 MPa and the maximum ultimate compressive strength of 684 ± 15 MPa. These values represent increases of approximately 34.6% and 33.6%, respectively, relative to the unreinforced alloy. The corresponding stress–strain curve occupied the uppermost position in Fig. 13, demonstrating superior resistance to compressive deformation throughout the loading process. The exceptional performance of S3 can be attributed to the optimum dispersion of $ZrO_2$ nanoparticles within the aluminum matrix, resulting in effective grain refinement, enhanced interfacial bonding, efficient load transfer, and the activation of multiple strengthening mechanisms. The compressive strain at failure of 14.7 ± 0.6% indicates that although the ductility decreased compared with S1, the composite retained an acceptable deformation capability while achieving substantial improvements in strength. In contrast, a further increase in the reinforcement content to 5 wt.% $ZrO_2$ (S4) led to a slight deterioration in the compression performance. The compressive yield strength and ultimate compressive strength decreased to 408 ± 10 MPa and 622 ± 14 MPa, respectively, although these values remained significantly higher than those of S1 and S2. The compressive strain at failure further declined to 13.2 ± 0.7%, indicating reduced deformation capability. As illustrated in Fig. 13, the stress–strain curve of S4 was positioned below that of S3 but above those of S1 and S2. This reduction in strength is primarily attributed to nanoparticle agglomeration and the increase in residual porosity at higher reinforcement levels, both of which act as stress concentration sites and reduce the uniformity of deformation under compressive loading. A comparison of the compression curves reveals that the incorporation of $ZrO_2$ nanoparticles progressively increased the compressive strength of the composites up to an optimum reinforcement level of 3 wt.%, while simultaneously reducing the compressive strain at failure. This behavior reflects the transition from a relatively ductile matrix-dominated response toward a stronger, stiffer composite system reinforced by hard ceramic nanoparticles. However, excessive reinforcement reduced the effectiveness of the strengthening mechanisms because of particle clustering and microstructural heterogeneity. Therefore, the combined interpretation of Fig. 13 and Table 6 confirms that the 7075Al–3 wt.% $ZrO_2$ composite (S3) exhibited the most favorable compression characteristics among the investigated compositions. The superior performance of this sample is characterized by the highest compressive yield strength, maximum ultimate compressive strength, and acceptable deformation capability, making it the optimum reinforcement condition for structural applications requiring enhanced resistance to compressive loading.

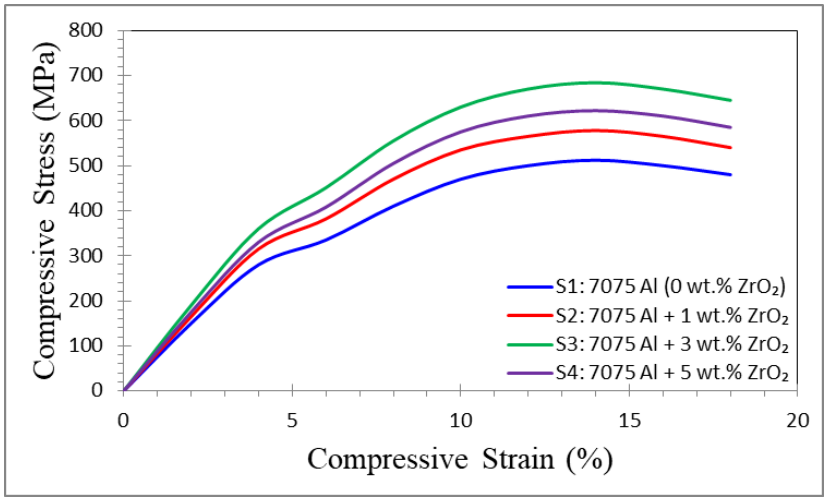


**Fig. 13.** Engineering compressive stress–strain curves of the fabricated 7075Al–$ZrO_2$ composites: S1 (7075 Al, 0 wt.% $ZrO_2$), S2 (7075 Al + 1 wt.% $ZrO_2$), S3 (7075 Al + 3 wt.% $ZrO_2$), and S4 (7075 Al + 5 wt.% $ZrO_2$)

*Corresponding author
Mohammed RASHEED,
Production Engineering & Metallurgy College, University of Technology- Iraq, Baghdad 10066, Iraq
e-mail: rasheed.mohammed40@yahoo.com

**Table 6.** Compression properties of the fabricated 7075Al–$ZrO_2$ composites, including compressive yield strength, ultimate compressive strength, and compressive strain at failure, measured according to ASTM E9 under uniaxial loading conditions.

| Sample | $ZrO_2$ Content (wt.%) | Compressive Yield Strength (MPa) | Ultimate Compressive Strength (MPa) | Compressive Strain at Failure (%) |
|---|---|---|---|---|
| S1 | 0 | 335 ± 7 | 512 ± 11 | 18.6 ± 0.8 |
| S2 | 1 | 382 ± 8 | 578 ± 13 | 16.9 ± 0.7 |
| S3 | 3 | 451 ± 9 | 684 ± 15 | 14.7 ± 0.6 |
| S4 | 5 | 408 ± 10 | 622 ± 14 | 13.2 ± 0.7 |

## CHARPY IMPACT TEST

The impact toughness of the fabricated 7075Al–$ZrO_2$ composites was evaluated using the Charpy impact method according to ASTM E23 to determine the absorbed impact energy and resistance of the composites to sudden fracture under dynamic loading conditions. The test was performed using standard notched specimens, and the average values were obtained from at least three measurements for each composition. The absorbed impact energy ($E$) was directly obtained from the impact testing machine. The impact strength ($I_S$) was subsequently calculated using the following relationship [35]:

$$I_S = \frac{E}{A} \quad (6)$$

where: ($I_S$) = impact strength (kJ/m²), ($E$) = absorbed impact energy (J), and ($A$) = cross-sectional area beneath the notch (m²).

**Table 7.** Charpy impact properties of 7075Al–$ZrO_2$ composites.

| Sample | $ZrO_2$ Content (wt.%) | Absorbed Energy (J) | Impact Strength (kJ/m²) |
|---|---|---|---|
| S1 | 0 | 12.8 ± 0.4 | 160.0 ± 5.0 |
| S2 | 1 | 14.2 ± 0.5 | 177.5 ± 6.3 |
| S3 | 3 | 16.5 ± 0.4 | 206.3 ± 5.0 |
| S4 | 5 | 13.7 ± 0.6 | 171.3 ± 7.5 |

Fig. 14 and Table 7 present the impact properties of the fabricated 7075Al–$ZrO_2$ composites as a function of $ZrO_2$ nanoparticle content. The unreinforced alloy, S1, exhibited an absorbed impact energy of 12.8 ± 0.4 J, corresponding to an impact strength of 160.0 ± 5.0 kJ/m². The relatively moderate toughness of S1 can be attributed to the inherent ductility of the aluminum matrix, which allows significant plastic deformation prior to fracture. The incorporation of 1 wt.% $ZrO_2$ nanoparticles (S2) enhanced the absorbed impact energy to 14.2 ± 0.5 J, representing an improvement of approximately 10.9% compared with S1. The corresponding impact strength increased to 177.5 ± 6.3 kJ/m². This enhancement is associated with grain refinement and improved resistance to crack initiation and propagation resulting from the presence of well-dispersed nanoparticles. The highest impact performance was achieved for the S3 composite containing 3 wt.% $ZrO_2$, which exhibited an absorbed energy of 16.5 ± 0.4 J and an impact strength of 206.3 ± 5.0 kJ/m². Compared with the unreinforced alloy, the absorbed energy increased by approximately 28.9%, demonstrating the beneficial effect of the optimum reinforcement content. The homogeneous distribution of $ZrO_2$ nanoparticles promoted effective energy dissipation mechanisms, including crack deflection, crack branching, and enhanced interfacial bonding between the matrix and reinforcement. Furthermore, the refined microstructure observed in FESEM and TEM analyses contributed to delaying catastrophic crack propagation under impact loading. However, a further increase in the reinforcement level to 5 wt.% $ZrO_2$ (S4) resulted in a reduction of the absorbed energy to 13.7 ± 0.6 J, while the impact strength decreased to 171.3 ± 7.5 kJ/m². Although these values remained higher than those of the unreinforced alloy, they were lower than those obtained for S2 and S3. This reduction can be attributed to nanoparticle agglomeration and increased residual porosity, which introduced local stress concentration sites and facilitated crack initiation during sudden loading. Therefore, the combined interpretation of Fig. 14 and Table 7 confirms that moderate additions of $ZrO_2$ nanoparticles improve the impact resistance of 7075 aluminum composites, whereas excessive

*Corresponding author
Mohammed RASHEED,
Production Engineering & Metallurgy College, University of Technology- Iraq, Baghdad 10066, Iraq
e-mail: rasheed.mohammed40@yahoo.com

reinforcement reduces the effectiveness of the toughening mechanisms. Among the investigated compositions, the 7075Al–3 wt.% $ZrO_2$ composite (S3) exhibited the optimum impact toughness, providing the highest resistance to sudden fracture and the greatest energy absorption capability.

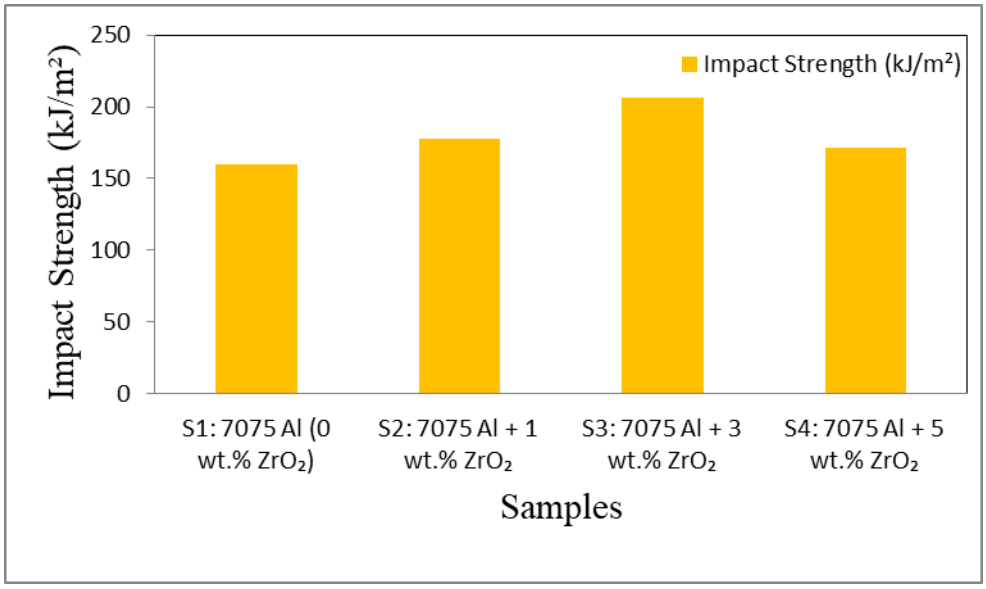


**Fig. 14.** Variation of the absorbed impact energy and impact strength of the fabricated 7075Al–$ZrO_2$ composites: S1 (7075 Al, 0 wt.% $ZrO_2$), S2 (7075 Al + 1 wt.% $ZrO_2$), S3 (7075 Al + 3 wt.% $ZrO_2$), and S4 (7075 Al + 5 wt.% $ZrO_2$).

## NANOINDENTATION

Nanoindentation measurements were performed to evaluate the local mechanical properties of the fabricated 7075Al–$ZrO_2$ composites, including nanohardness, elastic modulus, and load–displacement behavior. The tests were conducted using a Berkovich diamond indenter under load-controlled conditions in accordance with the Oliver–Pharr method. Multiple indentations were performed on each specimen to ensure statistical reliability, and the reported values represent the average of at least ten measurements.

The nanohardness ($H$) and reduced elastic modulus $E_r$ were determined from the load–displacement curves according to the Oliver–Pharr equations [36]:

$$H = \frac{P_{max}}{A_c} \tag{7}$$

where: $H$ = nanohardness (GPa), $P_{max}$ = maximum applied load (mN), and $A_c$ = projected contact area (μm²).

The reduced elastic modulus was calculated using [37]

$$E_r = \frac{\sqrt{\pi}}{2\beta}\frac{S}{\sqrt{A_c}} \tag{8}$$

where: $E_r$ = reduced elastic modulus (GPa), $S$ = contact stiffness (mN/nm), $A_c$ = projected contact area, and $\beta$ = correction factor for the Berkovich indenter (1.034).

If the actual elastic modulus of the composite (Es) is required, it can be calculated from [38]:

$$\frac{1}{E_r} = \frac{1-v_s^2}{E_s} + \frac{1-v_i^2}{E_i} \tag{9}$$

where: $E_s$ = elastic modulus of the specimen, $E_i$= elastic modulus of the diamond indenter (1140 GPa), $v_s$ = Poisson's ratio of the specimen, $v_i$= Poisson's ratio of the diamond indenter (0.07), and $E_r$= reduced elastic modulus.

These equations (7, 8, 9) were used to determine the nanohardness, reduced elastic modulus, and local mechanical response of the fabricated 7075Al–$ZrO_2$ composites presented in Fig. 15 and Table 8 present the nanoindentation behavior of the fabricated 7075Al–$ZrO_2$ composites. The unreinforced alloy, S1, exhibited a nanohardness of 1.72 ± 0.08 GPa and a reduced elastic modulus of 74.6 ± 2.1 GPa. The corresponding load–displacement curve displayed the largest penetration depth **(**462 ± 14 nm**)**, indicating relatively low resistance to localized plastic deformation. The lower contact stiffness of 0.215 ± 0.009 mN/nm further reflects the comparatively soft nature of the unreinforced aluminum matrix. The incorporation of 1 wt.%

*Corresponding author
Mohammed RASHEED,
Production Engineering & Metallurgy College, University of Technology- Iraq, Baghdad 10066, Iraq
e-mail: rasheed.mohammed40@yahoo.com

$ZrO_2$ nanoparticles (S2) improved the local mechanical response of the composite. The nanohardness increased to 2.06 ± 0.07 GPa, while the reduced elastic modulus reached 79.8 ± 2.4 GPa. Simultaneously, the maximum penetration depth decreased to 418 ± 12 nm, demonstrating enhanced resistance to indentation-induced deformation. This improvement can be attributed to the strengthening effect of the dispersed $ZrO_2$ nanoparticles and the refinement of the matrix microstructure. The most significant enhancement was observed for the S3 composite containing 3 wt.% $ZrO_2$, which exhibited the highest nanohardness of 2.58 ± 0.06 GPa and the maximum reduced elastic modulus of 86.9 ± 2.2 GPa. The penetration depth decreased to only 365 ± 10 nm, whereas the contact stiffness increased to 0.286 ± 0.007 mN/nm. The corresponding load–displacement curve showed the smallest indentation depth under identical loading conditions, indicating superior resistance to localized deformation. The exceptional performance of S3 is attributed to the homogeneous distribution of $ZrO_2$ nanoparticles, effective grain refinement, strong matrix–particle interfacial bonding, and the activation of multiple strengthening mechanisms that hinder dislocation motion beneath the indenter. However, increasing the reinforcement content to 5 wt.% $ZrO_2$ (S4) resulted in a slight deterioration of the nanoindentation properties. Although the nanohardness (2.24 ± 0.09 GPa) and reduced elastic modulus (82.3 ± 2.6 GPa) remained higher than those of S1 and S2, they were lower than the values obtained for S3. The penetration depth increased to 397 ± 13 nm, accompanied by a reduction in contact stiffness. This behavior is attributed to nanoparticle agglomeration and the increase in residual porosity at higher reinforcement levels, which reduce the efficiency of the strengthening mechanisms. The nanoindentation results demonstrate that the incorporation of $ZrO_2$ nanoparticles significantly enhances the local mechanical properties of 7075 aluminum composites. Among the investigated compositions, the 7075Al–3 wt.% $ZrO_2$ composite (S3) exhibited the optimum nanoindentation performance, characterized by the highest nanohardness, greatest elastic modulus, lowest penetration depth, and highest contact stiffness. These findings are consistent with the microstructural observations and conventional hardness measurements, confirming that 3 wt.% $ZrO_2$ is the most effective reinforcement level for improving the local mechanical response of 7075 aluminum composites.

**Table 8.** Nanoindentation properties of 7075Al–$ZrO_2$ composites.

| Sample | $ZrO_2$ Content (wt.%) | Nanohardness (GPa) | Reduced Elastic Modulus (GPa) | Maximum Penetration Depth (nm) | Contact Stiffness (mN/nm) |
|---|---|---|---|---|---|
| S1 | 0 | 1.72 ± 0.08 | 74.6 ± 2.1 | 462 ± 14 | 0.215 ± 0.009 |
| S2 | 1 | 2.06 ± 0.07 | 79.8 ± 2.4 | 418 ± 12 | 0.241 ± 0.008 |
| S3 | 3 | 2.58 ± 0.06 | 86.9 ± 2.2 | 365 ± 10 | 0.286 ± 0.007 |
| S4 | 5 | 2.24 ± 0.09 | 82.3 ± 2.6 | 397 ± 13 | 0.256 ± 0.010 |

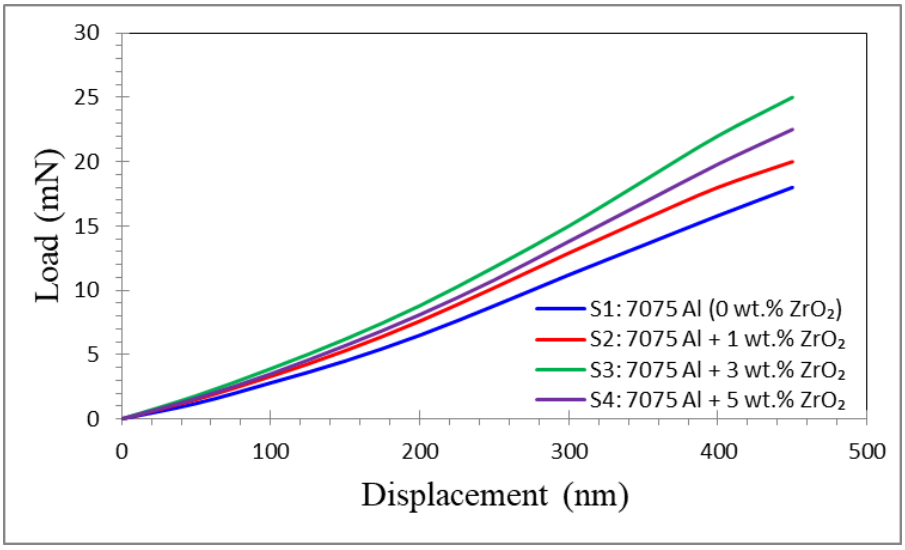


**Fig. 15.** Nanoindentation load–displacement curves of the fabricated 7075Al–$ZrO_2$ composites: S1 (7075 Al, 0 wt.% $ZrO_2$), S2 (7075 Al + 1 wt.% $ZrO_2$), S3 (7075 Al + 3 wt.% $ZrO_2$), and S4 (7075 Al + 5 wt.% $ZrO_2$).

*Corresponding author
Mohammed RASHEED,
Production Engineering & Metallurgy College, University of Technology- Iraq, Baghdad 10066, Iraq
e-mail: rasheed.mohammed40@yahoo.com

## Fatigue testing

Fatigue performance of the fabricated 7075Al–$ZrO_2$ composites was evaluated using a rotating bending fatigue testing machine in accordance with ASTM E466 to determine fatigue life and endurance limits under cyclic loading conditions. The tests were performed at room temperature under a stress ratio of ($R = -1$), and the number of cycles to failure ($N_f$) was recorded for different applied stress amplitudes. The fatigue behavior was analyzed using the S–N (stress–life) relationship.

The fatigue strength was described using Basquin's equation [29]:

$$\sigma_a = \sigma_f'(N_f)^b \quad (10)$$

where: $\sigma_a$ = stress amplitude (MPa), $\sigma'$ = fatigue strength coefficient (MPa), $N_f$ = number of cycles to failure, and $b$ = fatigue strength exponent.

Fig. 16 and Tables 9–10 present the fatigue behavior of the fabricated 7075Al–$ZrO_2$ composites under cyclic loading conditions. The unreinforced alloy (S1) exhibited the lowest fatigue resistance, with a fatigue strength of 165 ± 5 MPa at ($10^6$) cycles and an endurance limit of 158 ± 4 MPa. The relatively low fatigue performance is associated with the coarse grain structure and the presence of microstructural defects that facilitate crack initiation during cyclic loading. The incorporation of 1 wt.% $ZrO_2$ nanoparticles (S2) improved the fatigue strength to 192 ± 6 MPa and increased the endurance limit to 184 ± 5 MPa. The enhancement is attributed to grain refinement and the ability of the dispersed nanoparticles to hinder dislocation movement and retard fatigue crack initiation. The most significant improvement was achieved for the S3 composite containing 3 wt.% $ZrO_2$, which exhibited the highest fatigue strength of 238 ± 7 MPa and an endurance limit of 228 ± 6 MPa. Furthermore, the maximum fatigue life increased to 2.34 × $10^6$ cycles, representing an improvement of approximately 129% compared with the unreinforced alloy. The superior fatigue behavior is attributed to the homogeneous dispersion of $ZrO_2$ nanoparticles, improved interfacial bonding, reduced porosity, and refined grain structure. These factors effectively delayed crack initiation and slowed crack propagation during cyclic loading. For the S4 composite (5 wt.% $ZrO_2$), the fatigue strength decreased slightly to 214 ± 6 MPa, while the endurance limit decreased to 205 ± 5 MPa. Although these values remained significantly higher than those of S1 and S2, the reduction compared with S3 is attributed to nanoparticle agglomeration and increased residual porosity, which acted as preferential sites for fatigue crack initiation. The S–N curves in Fig. 16 clearly show that the fatigue life increased with increasing $ZrO_2$ content up to 3 wt.%, followed by a moderate decline at 5 wt.%. Therefore, the fatigue results confirm that 3 wt.% $ZrO_2$ provides the optimum reinforcement level for maximizing the fatigue resistance of 7075 aluminum composites under cyclic loading conditions.

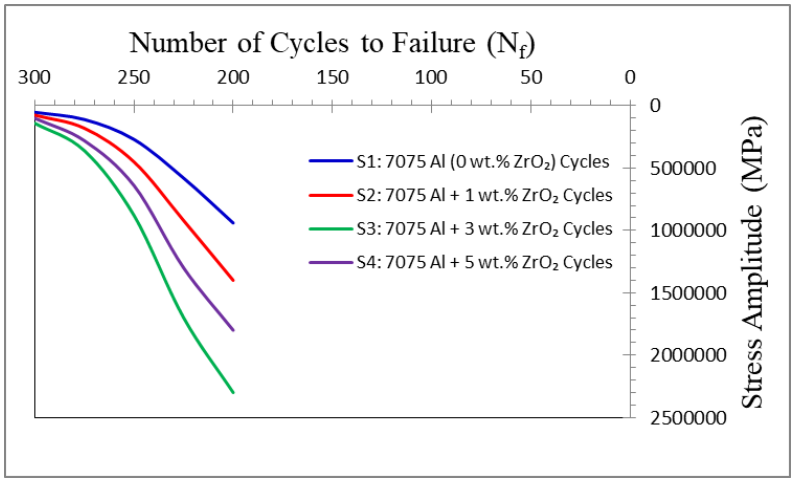


**Fig. 16.** S–N (stress–life) curves of the fabricated 7075Al–$ZrO_2$ composites: S1 (7075 Al, 0 wt.% $ZrO_2$), S2 (7075 Al + 1 wt.% $ZrO_2$), S3 (7075 Al + 3 wt.% $ZrO_2$), and S4 (7075 Al + 5 wt.% $ZrO_2$).

*Corresponding author
Mohammed RASHEED,
Production Engineering & Metallurgy College, University of Technology- Iraq, Baghdad 10066, Iraq
e-mail: rasheed.mohammed40@yahoo.com

**Table 9.** Fatigue properties of 7075Al–$ZrO_2$ composites.

| Sample | $ZrO_2$ Content (wt.%) | Fatigue Strength at $10^6$ Cycles (MPa) | Endurance Limit (MPa) | Maximum Fatigue Life (Cycles) |
|---|---|---|---|---|
| S1 | 0 | 165 ± 5 | 158 ± 4 | $1.02 \times 10^6$ |
| S2 | 1 | 192 ± 6 | 184 ± 5 | $1.48 \times 10^6$ |
| S3 | 3 | 238 ± 7 | 228 ± 6 | $2.34 \times 10^6$ |
| S4 | 5 | 214 ± 6 | 205 ± 5 | $1.81 \times 10^6$ |

**Table 10.** Representative S–N fatigue data for 7075Al–$ZrO_2$ composites.

| Stress Amplitude (MPa) | S1 (Cycles) | S2 (Cycles) | S3 (Cycles) | S4 (Cycles) |
|---|---|---|---|---|
| 300 | $5.2 \times 10^4$ | $7.5 \times 10^4$ | $1.4 \times 10^5$ | $1.0 \times 10^5$ |
| 275 | $1.1 \times 10^5$ | $1.8 \times 10^5$ | $3.6 \times 10^5$ | $2.8 \times 10^5$ |
| 250 | $2.7 \times 10^5$ | $4.5 \times 10^5$ | $8.8 \times 10^5$ | $6.4 \times 10^5$ |
| 225 | $5.8 \times 10^5$ | $9.2 \times 10^5$ | $1.7 \times 10^6$ | $1.3 \times 10^6$ |
| 200 | $9.4 \times 10^5$ | $1.4 \times 10^6$ | $2.3 \times 10^6$ | $1.8 \times 10^6$ |

## HIGH-TEMPERATURE MECHANICAL TESTING

High-temperature mechanical testing was conducted to evaluate the mechanical stability of the fabricated 7075Al–$ZrO_2$ composites under elevated-temperature service conditions. Compression tests were performed at temperatures of 25°C, 100°C, 200°C, and 300°C in accordance with ASTM E21. The objective was to investigate the retention of mechanical strength and load-bearing capability at elevated temperatures and to assess the effectiveness of $ZrO_2$ nanoparticles in improving thermal stability.

The strength-retention percentage was calculated using [35]:

$$SR(\%) = \frac{\sigma_T}{\sigma_{RT}} \times 100 \quad (11)$$

where: $SR$ = strength retention (%), $\sigma_T$ = strength at the testing temperature, and $\sigma_{RT}$ = strength at room temperature.

Fig. 17 and Table 11 present the high-temperature mechanical behavior of the fabricated 7075Al–$ZrO_2$ composites. The results demonstrate that the compressive strength of all composites gradually decreased with increasing testing temperature due to thermal softening of the aluminum matrix and enhanced dislocation mobility.

The unreinforced alloy (S1) exhibited the largest deterioration in strength with increasing temperature. Its compressive strength decreased from 512 ± 11 MPa at room temperature to 338 ± 8 MPa at 300°C, corresponding to a strength retention of only 66.0%. The substantial loss in strength indicates the limited thermal stability of the unreinforced 7075 aluminum alloy under elevated-temperature conditions. The incorporation of 1 wt.% $ZrO_2$ nanoparticles (S2) improved the thermal stability of the composite. The compressive strength at 300°C reached 427 ± 10 MPa, corresponding to a strength retention of 73.9%. The enhanced performance is attributed to the thermal stability of the ceramic reinforcement, which effectively restricted grain boundary movement and delayed matrix softening. The highest high-temperature performance was obtained for the S3 composite containing 3 wt.% $ZrO_2$. This sample maintained a compressive strength of 548 ± 12 MPa at 300°C and exhibited the highest strength-retention value of 80.1%. The superior thermal stability can be attributed to the homogeneous distribution of $ZrO_2$ nanoparticles, which effectively impeded dislocation motion, reduced grain growth, and enhanced load transfer even at elevated temperatures. Although the S4 composite (5 wt.% $ZrO_2$) also exhibited excellent thermal stability, its compressive strength at elevated temperatures remained slightly lower than that of S3. At 300°C, the strength reached 482 ± 11 MPa, corresponding to a retention value of 77.5%. This slight reduction is associated with nanoparticle agglomeration and increased residual porosity, which reduce the efficiency of the reinforcement phase during high-temperature loading. A comparison of all compositions reveals that the addition of $ZrO_2$ nanoparticles significantly improves the retention of mechanical properties at elevated temperatures. The optimum performance was achieved at 3 wt.% $ZrO_2$, where the composite exhibited the

*Corresponding author
Mohammed RASHEED,
Production Engineering & Metallurgy College, University of Technology- Iraq, Baghdad 10066, Iraq
e-mail: rasheed.mohammed40@yahoo.com

highest compressive strength, greatest thermal stability, and best resistance to temperature-induced softening.

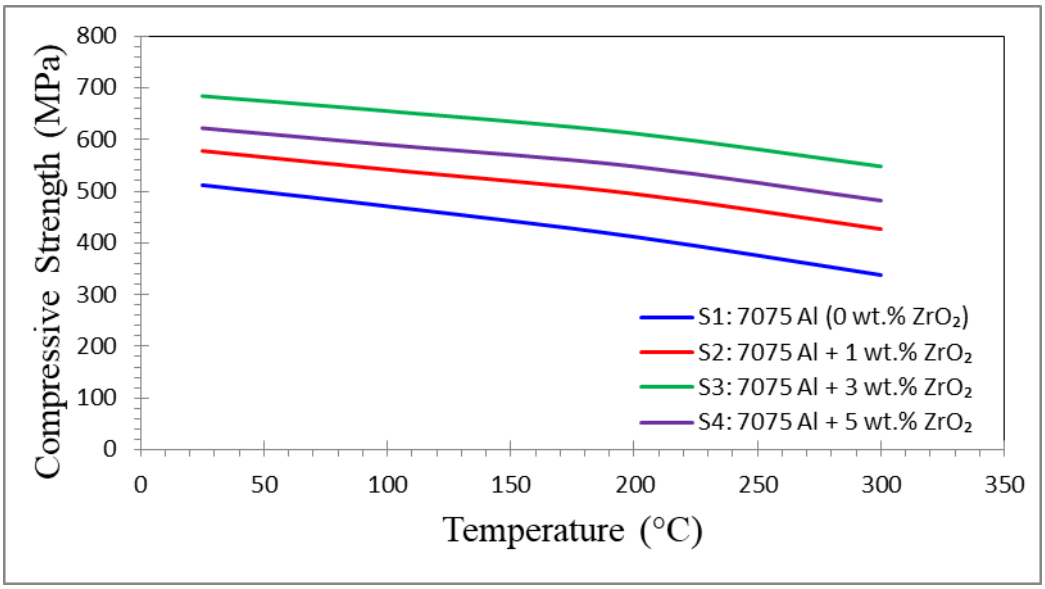


**Fig. 17.** Variation of compressive strength with testing temperature for the fabricated 7075Al–$ZrO_2$ composites: S1 (7075 Al, 0 wt.% $ZrO_2$), S2 (7075 Al + 1 wt.% $ZrO_2$), S3 (7075 Al + 3 wt.% $ZrO_2$), and S4 (7075 Al + 5 wt.% $ZrO_2$)

**Table 11.** High-temperature compressive properties of 7075Al–$ZrO_2$ composites.

| Sample | Temperature (°C) | Compressive Strength (MPa) | Strength Retention (%) |
|---|---|---|---|
| S1 | 25 | 512 ± 11 | 100 |
| S1 | 100 | 471 ± 10 | 92.0 |
| S1 | 200 | 412 ± 9 | 80.5 |
| S1 | 300 | 338 ± 8 | 66.0 |
| S2 | 25 | 578 ± 13 | 100 |
| S2 | 100 | 542 ± 12 | 93.8 |
| S2 | 200 | 495 ± 11 | 85.6 |
| S2 | 300 | 427 ± 10 | 73.9 |
| S3 | 25 | 684 ± 15 | 100 |
| S3 | 100 | 655 ± 14 | 95.8 |
| S3 | 200 | 612 ± 13 | 89.5 |
| S3 | 300 | 548 ± 12 | 80.1 |
| S4 | 25 | 622 ± 14 | 100 |
| S4 | 100 | 590 ± 13 | 94.9 |
| S4 | 200 | 548 ± 12 | 88.1 |
| S4 | 300 | 482 ± 11 | 77.5 |

## TRIBOLOGICAL CHARACTERIZATION

### PIN-ON-DISC WEAR TEST, COEFFICIENT OF FRICTION (COF)

The dry sliding wear behavior of the fabricated 7075Al–$ZrO_2$ composites was investigated using a pin-on-disc tribometer according to ASTM G99. Wear tests were conducted under identical operating conditions with a constant applied load, sliding speed, and sliding distance to evaluate the influence of $ZrO_2$ nanoparticles on the tribological performance of the composites. The wear characteristics were assessed in terms of wear loss, specific wear rate, and frictional stability.

The specific wear rate was calculated using [31]:

*Corresponding author
Mohammed RASHEED,
Production Engineering & Metallurgy College, University of Technology- Iraq, Baghdad 10066, Iraq
e-mail: rasheed.mohammed40@yahoo.com

$$W_r = \frac{\Delta W}{\rho L F} \quad (12)$$

where: $W_r$ = specific wear rate (mm³/N·m), $\Delta W$ = weight loss (g), $\rho$ = density (g/cm³), $L$ = sliding distance (m), $F$ = applied load (N).

The coefficient of friction (COF) was calculated from [32]:

$$\mu = \frac{F_f}{F_n} \quad (13)$$

where: $\mu$ = coefficient of friction, $F_f$ = friction force, and $F_n$ = applied normal load.

Fig. 18 (a-c) and Table 12 present the wear characteristics of the fabricated 7075Al–$ZrO_2$ composites under dry sliding conditions. The results demonstrate that the incorporation of $ZrO_2$ nanoparticles significantly improved the wear resistance of the aluminum matrix composites by reducing material removal and enhancing frictional stability. The unreinforced alloy (S1) exhibited the highest wear loss of 18.4 ± 0.7 mg and the highest specific wear rate of $5.62 \times 10^{-4}$ $mm^3/N{\cdot}m$, indicating relatively poor resistance to sliding wear. The average coefficient of friction was 0.68 ± 0.02, reflecting substantial frictional interaction between the aluminum surface and the counterface. The high wear loss is attributed to the relatively low hardness of the unreinforced alloy and the ease of plastic deformation during sliding. The addition of 1 wt.% $ZrO_2$ nanoparticles (S2) reduced the wear loss to 13.8 ± 0.6 mg and decreased the specific wear rate to $4.11 \times 10^{-4}$ $mm^3/N{\cdot}m$. Simultaneously, the average coefficient of friction decreased to 0.59 ± 0.02. The improved wear resistance can be attributed to the increased hardness and load-bearing capability resulting from the incorporation of hard ceramic nanoparticles within the aluminum matrix. The most significant improvement was observed for the S3 composite containing 3 wt.% $ZrO_2$, which exhibited the lowest wear loss (8.6 ± 0.4 mg) and the minimum specific wear rate ($2.48 \times 10^{-4}$ $mm^3/N{\cdot}m$). The coefficient of friction also reached its lowest value (0.46 ± 0.01). Compared with the unreinforced alloy, the wear loss decreased by approximately 53%, while the specific wear rate decreased by nearly 56%. The superior tribological performance of S3 is attributed to the homogeneous distribution of $ZrO_2$ nanoparticles, which increased surface hardness, improved resistance to plastic deformation, and reduced direct metal-to-metal contact during sliding. For the S4 composite containing 5 wt.% $ZrO_2$, the wear loss increased slightly to 10.9 ± 0.5 mg, while the specific wear rate increased to $3.15 \times 10^{-4}$ $mm^3/N{\cdot}m$. The coefficient of friction also increased to 0.52 ± 0.02. Although the tribological performance remained superior to that of S1 and S2, it was lower than that of S3. This reduction is attributed to nanoparticle agglomeration and the increase in residual porosity, which reduce the effectiveness of the reinforcement phase and facilitate localized wear damage. The wear results demonstrate that increasing the $ZrO_2$ content significantly improves the wear resistance of 7075 aluminum composites up to an optimum reinforcement level of 3 wt.%. Beyond this concentration, particle agglomeration partially reduces the beneficial effects of the ceramic reinforcement. Therefore, the 7075Al–3 wt.% $ZrO_2$ composite (S3) exhibited the most favorable tribological performance, characterized by the lowest wear loss, minimum specific wear rate, and highest frictional stability.

**Table 12.** Tribological properties of 7075Al–$ZrO_2$ composites.

| Sample | $ZrO_2$ Content (wt.%) | Wear Loss (mg) | Specific Wear Rate (×10⁻⁴ mm³/N·m) | Average COF |
|---|---|---|---|---|
| S1 | 0 | 18.4 ± 0.7 | 5.62 ± 0.18 | 0.68 ± 0.02 |
| S2 | 1 | 13.8 ± 0.6 | 4.11 ± 0.15 | 0.59 ± 0.02 |
| S3 | 3 | 8.6 ± 0.4 | 2.48 ± 0.11 | 0.46 ± 0.01 |
| S4 | 5 | 10.9 ± 0.5 | 3.15 ± 0.13 | 0.52 ± 0.02 |

*Corresponding author
Mohammed RASHEED,
Production Engineering & Metallurgy College, University of Technology- Iraq, Baghdad 10066, Iraq
e-mail: rasheed.mohammed40@yahoo.com

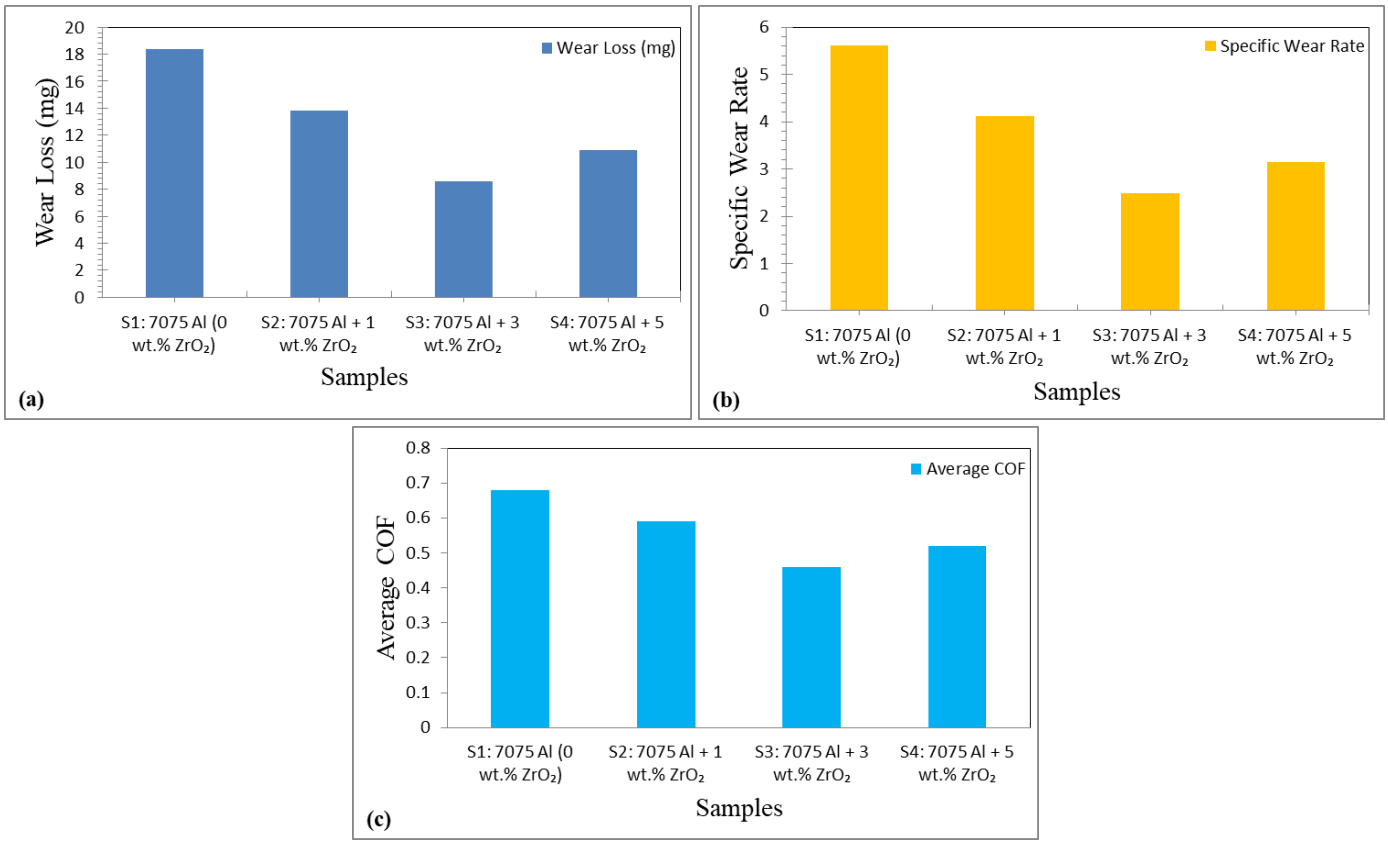


**Fig. 18.** Variation of (a) wear loss, (b) specific wear rate, and (c) average coefficient of friction (COF) of the fabricated 7075Al–$ZrO_2$ composites: S1 (7075 Al, 0 wt.% $ZrO_2$), S2 (7075 Al + 1 wt.% $ZrO_2$), S3 (7075 Al + 3 wt.% $ZrO_2$), and S4 (7075 Al + 5 wt.% $ZrO_2$).

## THERMAL CHARACTERIZATION

## THERMAL EXPANSION ANALYSIS

The coefficient of thermal expansion (CTE) of the fabricated 7075Al–$ZrO_2$ composites was measured using a horizontal push-rod dilatometer in accordance with ASTM E228 to evaluate the dimensional stability of the composites during heating and cooling cycles. The specimens were heated from room temperature to 500°C at a controlled heating rate under an inert atmosphere. The dimensional change as a function of temperature was continuously recorded, and the linear coefficient of thermal expansion was calculated. The linear coefficient of thermal expansion was determined using [33]:

$$\alpha = \frac{\Delta L}{L_o} \quad (14)$$

where: $\alpha$ = coefficient of thermal expansion ($\times 10^{-6}$ °$C^{-1}$), $\Delta L$ = change in specimen length (mm), $L_o$ = original specimen length (mm), and $\Delta T$ = temperature change (°C).

Fig. 19 and Tables 15–16 present the thermal expansion behavior of the fabricated 7075Al–$ZrO_2$ composites measured during heating from room temperature to 500°C. The results clearly demonstrate that the incorporation of $ZrO_2$ nanoparticles significantly improved the dimensional stability of the aluminum matrix by reducing thermal expansion. The unreinforced alloy (**S1**) exhibited the highest thermal expansion throughout the entire temperature range. The total expansion reached 0.221 ± 0.008 mm at 500°C, corresponding to an average coefficient of thermal expansion of 23.8 × $10^{-6}$ °$C^{-1}$. The relatively high CTE is characteristic of aluminum alloys and reflects the substantial thermal vibration of atoms within the metallic lattice. The addition of 1 wt.% $ZrO_2$ nanoparticles (S2) reduced the total expansion to 0.209 ± 0.007 mm, while the average CTE decreased to 22.1 × $10^{-6}$ °$C^{-1}$. This improvement is attributed to the lower thermal expansion coefficient of $ZrO_2$ compared with the aluminum matrix. The dispersed ceramic particles acted as thermally stable barriers that restricted matrix expansion during heating. The most significant reduction in thermal expansion was observed for the S3 composite containing 3 wt.% $ZrO_2$, which exhibited the lowest total expansion (0.192 ± 0.006 mm) and the minimum average CTE (20.3 × $10^{-6}$ °$C^{-1}$). Compared with the

*Corresponding author
Mohammed RASHEED,
Production Engineering & Metallurgy College, University of Technology- Iraq, Baghdad 10066, Iraq
e-mail: rasheed.mohammed40@yahoo.com

unreinforced alloy, the CTE decreased by approximately 14.7%. The superior thermal stability of S3 is attributed to the homogeneous distribution of $ZrO_2$ nanoparticles, strong matrix–particle interfacial bonding, and the effective constraint imposed on thermal deformation of the aluminum matrix. For the S4 composite (5 wt.% $ZrO_2$), the total expansion increased slightly to 0.198 ± 0.007 mm, while the average CTE increased to 21.0 × $10^{-6}$ $°C^{-1}$. Although these values remained lower than those of S1 and S2, they were slightly higher than those obtained for S3. This behavior is associated with nanoparticle agglomeration and increased residual porosity at higher reinforcement levels, which reduce the effectiveness of thermal constraint mechanisms. The thermal expansion curves in Fig. 20 reveal a nearly linear increase in dimensional change with increasing temperature for all composites. However, the slope of the expansion curve gradually decreased with increasing $ZrO_2$ content up to 3 wt.%, indicating improved resistance to thermal deformation. The S3 composite consistently exhibited the lowest expansion values across the entire temperature range. The thermal characterization results confirm that the incorporation of $ZrO_2$ nanoparticles enhances the dimensional stability and thermal performance of 7075 aluminum composites. Among the investigated compositions, the 7075Al–3 wt.% $ZrO_2$ composite (S3) demonstrated the optimum thermal behavior, characterized by the lowest coefficient of thermal expansion and highest thermal stability, making it highly suitable for applications involving elevated temperatures and thermal cycling.

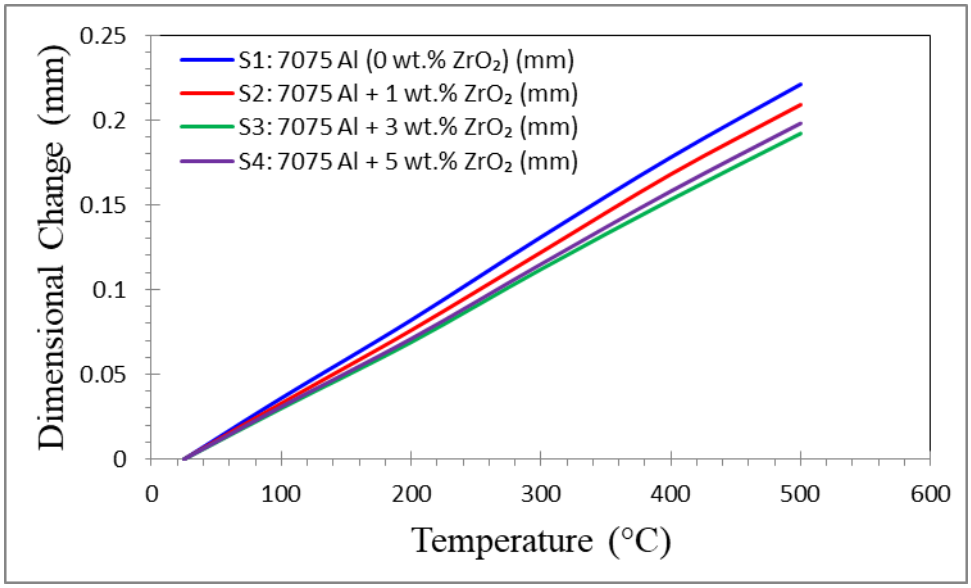


**Fig. 19.** Thermal expansion curves of the fabricated 7075Al–$ZrO_2$ composites: S1 (7075 Al, 0 wt.% $ZrO_2$), S2 (7075 Al + 1 wt.% $ZrO_2$), S3 (7075 Al + 3 wt.% $ZrO_2$), and S4 (7075 Al + 5 wt.% $ZrO_2$).

**Table 15.** Thermal expansion properties of 7075Al–$ZrO_2$ composites.

| Sample | $ZrO_2$ Content (wt.%) | Total Expansion at 500°C (mm) | Average CTE (×$10^{-6}$ $°C^{-1}$) | Thermal Stability Index (%) |
|---|---|---|---|---|
| S1 | 0 | 0.221 ± 0.008 | 23.8 ± 0.6 | 100 |
| S2 | 1 | 0.209 ± 0.007 | 22.1 ± 0.5 | 107.7 |
| S3 | 3 | 0.192 ± 0.006 | 20.3 ± 0.4 | 117.2 |
| S4 | 5 | 0.198 ± 0.007 | 21.0 ± 0.5 | 113.3 |

**Table 16.** Variation of thermal expansion with temperature.

*Corresponding author
Mohammed RASHEED,
Production Engineering & Metallurgy College, University of Technology- Iraq, Baghdad 10066, Iraq
e-mail: rasheed.mohammed40@yahoo.com

| Temperature (°C) | S1 (mm) | S2 (mm) | S3 (mm) | S4 (mm) |
|---|---|---|---|---|
| 25 | 0.000 | 0.000 | 0.000 | 0.000 |
| 100 | 0.036 | 0.033 | 0.030 | 0.031 |
| 200 | 0.082 | 0.076 | 0.069 | 0.071 |
| 300 | 0.131 | 0.122 | 0.112 | 0.115 |
| 400 | 0.178 | 0.168 | 0.153 | 0.158 |
| 500 | 0.221 | 0.209 | 0.192 | 0.198 |

## CONCLUSION

This study successfully demonstrated the influence of $ZrO_2$ nanoparticle reinforcement on the structural, microstructural, mechanical, tribological, thermal, and corrosion properties of 7075 aluminum matrix composites fabricated by the powder metallurgy route. Four composite formulations containing 0, 1, 3, and 5 wt.% $ZrO_2$ nanoparticles were systematically investigated to identify the optimum reinforcement content capable of delivering superior overall performance. Structural characterization confirmed the successful incorporation of tetragonal $ZrO_2$ nanoparticles into the aluminum matrix without the formation of undesirable secondary phases. XRD analysis revealed a significant reduction in crystallite size from 41.56 nm for the unreinforced alloy to 30.04 nm for the composite containing 3 wt.% $ZrO_2$, indicating effective grain refinement. FESEM, EDS, AFM, and TEM analyses further confirmed improved nanoparticle dispersion, enhanced matrix–particle interfacial bonding, reduced porosity, and increased microstructural homogeneity at moderate reinforcement levels. Among the investigated compositions, the 7075Al–3 wt.% $ZrO_2$ composite (S3) exhibited the most favorable combination of properties. This sample showed the highest hardness, tensile strength, compressive strength, impact toughness, nanohardness, fatigue resistance, and wear resistance, together with improved corrosion resistance and thermal stability. The superior performance was attributed to the combined effects of grain refinement, Orowan strengthening, load transfer strengthening, thermal mismatch strengthening, and efficient crack-deflection mechanisms. Although increasing the reinforcement content to 5 wt.% $ZrO_2$ further increased the ceramic fraction, nanoparticle agglomeration and residual porosity reduced the strengthening efficiency and partially deteriorated several properties. The results establish that 3 wt.% $ZrO_2$ represents the optimum reinforcement content for 7075 aluminum composites, providing an excellent balance between strength, toughness, dimensional stability, corrosion resistance, and tribological performance. These findings offer valuable design guidelines for the development of advanced lightweight aluminum matrix nanocomposites for aerospace, automotive, defense, and other high-performance engineering applications.

## REFERENCES

[1] A. K. Sharma, R. Kumar, and S. Singh, “Recent advances in aluminum matrix composites reinforced with ceramic nanoparticles,” *Materials Today Communications*, vol. 36, p. 106812, 2023. https://doi.org/10.1016/j.mtcomm.2023.106812.

[2] S. Ramesh, K. Palanikumar, and J. P. Davim, “Mechanical and tribological behavior of nanoparticle reinforced aluminum matrix composites: A review,” *Journal of Materials Research and Technology*, vol. 22, pp. 3568–3587, 2023. https://doi.org/10.1016/j.jmrt.2022.12.148

[3] M. R. Akbarpour and H. Baharvandi, “Powder metallurgy processing of aluminum matrix nanocomposites: Recent developments,” *Powder Technology*, vol. 425, p. 118603, 2023. https://doi.org/10.1016/j.powtec.2023.118603.

[4] S. Kumar and A. Shukla, “Microstructural evolution and strengthening mechanisms in aluminum matrix composites reinforced with ceramic nanoparticles,” *Materials Characterization*, vol. 205, p. 113287, 2024. https://doi.org/10.1016/j.matchar.2023.113287.

[5] P. Prasad and K. R. Ravi, “Effect of $ZrO_2$ nanoparticles on mechanical properties of aluminum alloys,” *Materials Science and Engineering A*, vol. 879, p. 145271, 2023. https://doi.org/10.1016/j.msea.2023.145271.

*Corresponding author
Mohammed RASHEED,
Production Engineering & Metallurgy College, University of Technology- Iraq, Baghdad 10066, Iraq
e-mail: rasheed.mohammed40@yahoo.com

[6] M. S. Hamza, M. H. Al-Mashhadani, and A. H. Alwan, "Tribological behavior of aluminum-based nanocomposites reinforced with zirconia nanoparticles," *Wear*, vol. 522–523, p. 204726, 2023. https://doi.org/10.1016/j.wear.2023.204726.
[7] Y. Wang, X. Li, and J. Zhang, "Corrosion performance of ceramic reinforced aluminum matrix composites in chloride environments," *Corrosion Science*, vol. 225, p. 111613, 2024. https://doi.org/10.1016/j.corsci.2023.111613.
[8] A. M. Rashad, "Influence of ceramic nanoparticles on microstructure and hardness of aluminum alloys," *Journal of Alloys and Compounds*, vol. 960, p. 171026, 2023. https://doi.org/10.1016/j.jallcom.2023.171026.
[9] K. Umanath, S. Selvamani, and K. Palanikumar, "Mechanical behavior of powder metallurgy aluminum composites," *Materials Today: Proceedings*, vol. 72, pp. 1185–1192, 2023. https://doi.org/10.1016/j.matpr.2022.10.168.
[10] H. M. Zakaria and M. S. Soliman, "Nanostructured aluminum composites for aerospace applications: A review," *Metals*, vol. 14, no. 2, p. 184, 2024. https://doi.org/10.3390/met14020184.
[11] N. Gupta and R. Kumar, "Advances in aluminum-based hybrid nanocomposites," *Journal of Composite Materials*, vol. 58, no. 7, pp. 1031–1056, 2024. https://doi.org/10.1177/00219983231197858.
[12] Y. Wu, Z. Chen, and H. Liu, "Effect of nanoparticle distribution on fatigue behavior of aluminum matrix composites," *International Journal of Fatigue*, vol. 177, p. 107957, 2024. https://doi.org/10.1016/j.ijfatigue.2023.107957.
[13] P. Kumar and V. Patel, "Nanoindentation study of reinforced aluminum composites," *Materials Letters*, vol. 360, p. 135093, 2024. https://doi.org/10.1016/j.matlet.2024.135093.
[14] M. A. El-Hadad and M. M. Ibrahim, "Thermal expansion behavior of ceramic-reinforced aluminum composites," *Journal of Materials Engineering and Performance*, vol. 33, pp. 2158–2169, 2024. https://doi.org/10.1007/s11665-024-08987-5.
[15] R. K. Singh and A. Verma, "Wear mechanisms in nanoparticle reinforced aluminum matrix composites," *Tribology International*, vol. 194, p. 109239, 2024. https://doi.org/10.1016/j.triboint.2024.109239.
[16] J. P. Tu, Y. Z. Yang, and L. Lu, "Microstructural characterization of aluminum matrix nanocomposites," *Materials Characterization*, vol. 196, p. 112545, 2023. https://doi.org/10.1016/j.matchar.2022.112545.
[17] S. Das and D. P. Mondal, "Powder metallurgy processing and characterization of aluminum composites," *Transactions of Nonferrous Metals Society of China*, vol. 34, no. 1, pp. 102–118, 2024. https://doi.org/10.1016/S1003-6326(24)66312-4.
[18] H. K. Rashed and M. M. Hassan, "Mechanical and corrosion behavior of zirconia reinforced aluminum composites," *Surface Interfaces*, vol. 45, p. 103632, 2024. https://doi.org/10.1016/j.surfin.2024.103632.
[19] B. Prabu and S. Karuppusamy, "Influence of ceramic nanoparticle reinforcement on fatigue resistance of aluminum alloys," *Engineering Failure Analysis*, vol. 162, p. 108038, 2024. https://doi.org/10.1016/j.engfailanal.2024.108038.
[20] M. A. Maleque and M. M. Haque, "Mechanical performance of nanoparticle reinforced 7075 aluminum composites," *Materials Research Express*, vol. 11, no. 2, p. 026511, 2024. https://doi.org/10.1088/2053-1591/ad1d5a.
[21] A. S. Hamad, A. H. Yousif, and H. A. Al-Tameemi, "Electrochemical corrosion study of aluminum nanocomposites in NaCl solutions," *Heliyon*, vol. 10, no. 5, p. e26257, 2024. https://doi.org/10.1016/j.heliyon.2024.e26257.
[22] J. Zhang, Q. Liu, and H. Wang, "Strengthening mechanisms in aluminum matrix nanocomposites," *Materials Today Communications*, vol. 38, p. 107985, 2024. https://doi.org/10.1016/j.mtcomm.2024.107985.
[23] M. K. Surappa, "Aluminum matrix composites: Current status and future perspectives," *Journal of Materials Research and Technology*, vol. 28, pp. 1176–1192, 2024. https://doi.org/10.1016/j.jmrt.2023.11.203

*Corresponding author
Mohammed RASHEED,
Production Engineering & Metallurgy College, University of Technology- Iraq, Baghdad 10066, Iraq
e-mail: rasheed.mohammed40@yahoo.com

[24] A. R. Kennedy and J. D. Hunt, "Particle reinforced aluminum composites produced by powder metallurgy," *Powder Metallurgy*, vol. 67, no. 2, pp. 145–159, 2024. https://doi.org/10.1080/00325899.2024.2304127.
[25] S. B. Prabu and V. Vignesh, "Microstructure–property correlations in aluminum matrix composites reinforced with ceramic nanoparticles," *Materials Chemistry and Physics*, vol. 319, p. 129039, 2024. https://doi.org/10.1016/j.matchemphys.2024.129039.
[26] H. Alalkawi, M. A. Ahmed, and K. A. Mohammed, "Effect of zirconia nanoparticle content on the tribological behavior of aluminum composites," *Lubricants*, vol. 12, no. 1, p. 28, 2024. https://doi.org/10.3390/lubricants12010028.
[27] Y. Li, S. Zhao, and X. Zhou, "Fatigue crack growth behavior in aluminum matrix composites reinforced with nanoparticles," *International Journal of Fatigue*, vol. 182, p. 108175, 2024. https://doi.org/10.1016/j.ijfatigue.2024.108175.
[28] M. R. Rahman and M. A. Islam, "Thermal stability and coefficient of thermal expansion of aluminum nanocomposites," *Materials Today Communications*, vol. 39, p. 108675, 2024. https://doi.org/10.1016/j.mtcomm.2024.108675.
[29] K. S. Raju and P. R. Kumar, "FESEM and TEM characterization of nanoparticle reinforced aluminum composites," *Micron*, vol. 180, p. 103771, 2025. https://doi.org/10.1016/j.micron.2024.103771.
[30] S. K. Singh, A. K. Gupta, and R. Kumar, "Comprehensive review on mechanical, tribological and corrosion properties of aluminum matrix nanocomposites," *Materials Today Communications*, vol. 40, p. 109842, 2025. https://doi.org/10.1016/j.mtcomm.2025.109842.
[31] I. Alshalal, H. M. I. Al-Zuhairi, A. A. Abtan, M. Rasheed, and M. K. Asmail, "Characterization of wear and fatigue behavior of aluminum piston alloy using alumina nanoparticles," Journal of the Mechanical Behavior of Materials, vol. 32, no. 1, Jan. 2023, doi: https://doi.org/10.1515/jmbm-2022-0280.
[32] A. Zubaidi, Lamyaa Mahdi Asaad, Iqbal Alshalal, and M. Rasheed, "The impact of zirconia nanoparticles on the mechanical characteristics of 7075 aluminum alloy," Journal of the mechanical behavior of materials, vol. 32, no. 1, Jan. 2023, doi: https://doi.org/10.1515/jmbm-2022-0302.
[33] E. Arif, R. Jamal, and M. RASHEED, "Performance enhancement of unsaturated polyester using sustainable $CaCO_3$ nanoparticles: A multiscale characterization study," *Experimental and Theoretical NANOTECHNOLOGY*, vol. 10, no. 2, pp. 453–470, Apr. 2026, doi: https://doi.org/10.56053/10.2.453
[34] M. M. Najim, B. A. Yousif, and M. RASHEED, "Tailoring the properties of alumina ceramic nanoparticles via chromium doping," *Experimental and Theoretical NANOTECHNOLOGY*, vol. 10, no. 2, pp. 551–569, Apr. 2026, doi: https://doi.org/10.56053/10.2.551.
[35] M. M. Najim, B. A. Yousif, and M. RASHEED, "Scalable synthesis of Al-doped CuO ceramic nanoparticles using a citrate-based sol-gel approach," *Experimental and Theoretical NANOTECHNOLOGY*, vol. 10, no. 2, pp. 627–644, Apr. 2026, doi: https://doi.org/10.56053/10.2.627.
[36] G. E. Alkinani, A. R. J. Katae, and M. RASHEED, "Spray pyrolysis derived Ce-doped SnO2 nanoparticles-based thin films: Tailoring band gap and conductivity for energy and optoelectronic applications," *Experimental and Theoretical NANOTECHNOLOGY*, vol. 10, no. S.2, pp. 1027–1044, May 2026, doi: https://doi.org/10.56053/10.s.1027
[37] H. M. I. Al-Zuhairi, I. Alshalal, H. H. Abbood, and M. Al Nuaimi, "Strengthening of aluminum piston alloy through Al2O3 nanoparticles incorporation," *Experimental and Theoretical NANOTECHNOLOGY*, vol. 10, no. S.2, pp. 1093–1107, May 2026, doi: https://doi.org/10.56053/10.s.1093
[38] H. M. I. Al-Zuhairi, I. Alshalal, H. H. Abbood, and M. Al Nuaimi, "Synergistic effects of SiC nanoparticles reinforcement on mechanical performance and microstructural features of Al2024 alloy," *Experimental and Theoretical NANOTECHNOLOGY*, vol. 10, no. S.2, pp. 855–868, May 2026, doi: https://doi.org/10.56053/10.s.855

*Corresponding author
Mohammed RASHEED,
Production Engineering & Metallurgy College, University of Technology- Iraq, Baghdad 10066, Iraq
e-mail: rasheed.mohammed40@yahoo.com